



University of
Stavanger

Faculty of Science and Technology

MASTER'S THESIS

Study program/Specialization: Mathematics and physics	Spring semester, 2021 Open
Writer: Amanda Lavinia Kjærnsmo	<i>Amanda L. Kjærnsmo</i> (Writer's signature)
Faculty supervisor: Aleksi Kurkela	
Thesis title: Quantum chromodynamics and particle energy-loss in heavy-ion collisions due to medium interactions.	
Credits (ECTS): 60	
Key words: Quantum chromodynamics, group theory, field theory, heavy-ion collisions, quark-gluon plasma	Pages: 71 + enclosure: none Stavanger, June 15, 2021 Date/year

Quantum chromodynamics and particle energy-loss
in heavy-ion collisions due to medium interactions.

Author: Amanda Lavinia Kjærnsmo

Supervisor: Aleksi Kurkela

June 15, 2021

Contents

Introduction	3
1 Quantum Chromodynamics	5
1.1 Lie Groups	5
1.2 Theory of the strong interaction	9
1.3 Quark-Gluon Plasma	12
1.4 Perfect fluid	14
2 QCD: Derivations	16
2.1 Action on the lattice	16
2.2 The Gluon propagator	19
2.3 Attractive and repulsive interactions	22
2.4 Feynman rules for the gluon vertices	25
2.4.1 Triple-gluon vertex	25
2.4.2 Four-gluon vertex	27
3 Heavy-ion collisions	29
3.1 Evolution of the collision	29
3.2 Observables	31
3.2.1 Elliptic flow	31
3.2.2 Nuclear modification factor, R_{AA}	33
3.2.3 Jet-suppression	35
3.2.4 Strangeness enhancement	38
4 Energy-loss of a particle travelling through a medium	40
4.1 Medium-induced gluon radiation	40
4.2 The "brick" (uniform, time-independent medium)	42
4.2.1 Asymptotic solutions	43

4.3	From medium-induced radiation spectrum to the energy-loss of a particle	48
4.4	Power-law (time-dependent medium)	51
4.5	Comparing different mediums: Brick vs. Power-law	56
4.6	Scaling laws	58
4.6.1	Salgado and Wiedemann	59
4.6.2	Small ω scaling	59
4.6.3	Large ω scaling	61
4.6.4	Comparing different scaling laws	64
	Summary and Outlook	66
	Acknowledgements	68
	Bibliography	68

Introduction

This thesis is a study of medium-induced particle energy-loss, which occur in heavy-ion collisions where quark-gluon plasma (QGP) is created. Quantum chromodynamics (QCD), the theory of strong interactions, is the underlying theory of the following. Therefore, the first half of this paper is dedicated to the introduction and derivation of several interesting results of this theory.

Quantum chromodynamics is a non-Abelian theory. To better understand what this means, an introduction to group theory is included in Chapter 1. The rest of the chapter includes a short introduction as well as commonly used terminology in QCD. Chapter 2 contains some detailed derivations. First, the action on the lattice is connected to the Yang-Mills action. Then, the gluon propagator is derived and compared to that of the photon propagator used in quantum electrodynamics (QED). A short study of the interaction of quarks are made to find out whether these are attractive or repulsive. Lastly, the Feynman diagrams involving the 3- and 4-point gluon vertices, arising from the colour charge, are derived.

In Chapter 3, I will look at the time evolution of heavy-ion collisions and the observed elliptic flow, nuclear modification factor, jet-suppression and strangeness enhancement. We will see how these observables suggest the production of quark-gluon plasma in heavy-ion collisions.

In Chapter 4, I follow the work done by Arnold [1] and use his result for predicting the energy-loss of a particle travelling through a finite medium. The study starts by understanding how a particle loses energy due to medium interactions in a "simple", time-independent medium profile referred to as the brick. Most of the medium-induced radiation will be to soft gluon emissions carrying energy/frequency, $\omega < \omega_{cr}$. The critical value, ω_{cr} , is defined as the intersection point of the two asymptotic solutions of the gluon emission spectrum. Emitting a gluon of higher energy than this value is possible, but does not happen as frequently as in the low ω -regime.

Next, a more complicated medium, which depends on time via the power-law, $\propto 1/t^a$, is considered. A general formula for the asymptotic behaviour of the spectrum is applied. A quick dimensional analysis suggests that for values of $a > 2$, the spectrum follows closely that of the small L expansion (see Section 4.4). This is due to the fact that the medium effects drops fast enough for it to look like a small system.

Lastly, a comparison of the two medium profiles are made and connected via the use of a scaling law (Section 4.6). A scaling law let us find the gluon emission spectrum of a time-dependent medium using the simpler solution of the brick. Three different scaling laws are considered: one provided by Salgado and Wiedemann [2] and two derived by me. I connect the scaling laws to the analytical solution found by [1] and compare their accuracy. This is the first time such a comparison has been done, as far as I know. The scaling law provided by Salgado and Wiedemann is easy to use and gives a good approximation to the time-dependent spectrum. One of the scaling laws derived in this paper shows an even smaller deviation from the time-dependent spectrum for energies $\omega > 0.65\omega_{cr}$ (approximate vale). It will be shown that the total energy-loss of a particle depends on the value of ω_{cr} . Thus, if one is interested in the spectrum around ω_{cr} or higher energies, the scaling law derived in this paper gives a better fit than the one provided by Salgado and Wiedemann.

The following will be done in natural units, for which $c = \hbar = 1$.

Chapter 1

Quantum Chromodynamics

In this chapter, a short introduction to quantum chromodynamics (QCD) is given. Terminology often used in this theory, such as color charge, confinement and asymptotic freedom, is explained. The strong interaction is described by quantum chromodynamics which is a non-Abelian group theory. To understand what a non-Abelian group theory is, we need to have an insight to the mathematics behind Lie groups. A small introduction to group theory is thus included to understand some of the mathematics that lies behind the theory. The important multiplication rule of the Lie group, the Lie bracket, is defined and the Casimir is introduced. For simplicity, examples of these are made using the group $SU(2)$. However, since the group describing QCD is $SU(3)$, a simpler way of determining the Casimir of any group in $SU(N)$ is also provided.

Quark-gluon plasma (QGP) and the concept of a perfect fluid is mentioned in the last part of this chapter. QGP filled the early universe, and small droplets of this is created in heavy-ion collisions. So far, it is the closest we have come to find a perfect fluid. The study of heavy-ion collisions provide more insight to the strong interaction acting between coloured particles and the properties of QGP which can be derived from the observables.

1.1 Lie Groups

In this section, a short introduction to some of the most important parts of group theory connected to particle physics is given. This section is inspired by [3, p.159-160, 481-488]. The main focus will be on the special unitary group, $SU(N)$. $SU(2)$

describes the theory of weak interactions and are generated by the Pauli spin matrices, σ^a . These are used in quantum mechanics to describe the spin of fundamental particles and are given by

$$\sigma^1 = \begin{pmatrix} 0 & 1 \\ 1 & 0 \end{pmatrix}, \quad \sigma^2 = \begin{pmatrix} 0 & -i \\ i & 0 \end{pmatrix}, \quad \sigma^3 = \begin{pmatrix} 1 & 0 \\ 0 & -1 \end{pmatrix}. \quad (1.1)$$

Quantum chromodynamics is described by the group SU(3), generated by the traceless, hermitean Gell-Mann matrices, λ^a , given by

$$\begin{aligned} \lambda^1 &= \begin{pmatrix} 0 & 1 & \\ 1 & 0 & \\ & & 0 \end{pmatrix}, & \lambda^2 &= \begin{pmatrix} 0 & i & \\ i & 0 & \\ & & 0 \end{pmatrix}, & \lambda^3 &= \begin{pmatrix} 1 & & \\ & -1 & \\ & & 0 \end{pmatrix}, \\ \lambda^4 &= \begin{pmatrix} & & 1 \\ & 0 & \\ 1 & & \end{pmatrix}, & \lambda^5 &= \begin{pmatrix} 0 & & -i \\ & 0 & \\ i & & 0 \end{pmatrix}, & \lambda^6 &= \begin{pmatrix} 0 & & \\ & 0 & 1 \\ & 1 & 0 \end{pmatrix}, \\ \lambda^7 &= \begin{pmatrix} 0 & & \\ & 0 & -i \\ & i & 0 \end{pmatrix}, & \lambda^8 &= \frac{1}{\sqrt{3}} \begin{pmatrix} 1 & & \\ & 1 & \\ & & -2 \end{pmatrix}. \end{aligned} \quad (1.2)$$

A group is a set of elements $\{g_i\}$ and a rule which describes how a binary operation "x" between two elements produces a third, $g_i \times g_j = g_k$. The rule must be associative, $(g_i \times g_j) \times g_k = g_i \times (g_j \times g_k)$, the group must have an identity element, $g_i \times \mathbb{1} = \mathbb{1} \times g_i = g_i$, and each element has an inverse such that $g_i^{-1} \times g_i = \mathbb{1}$ [3, p.159]. A Lie group is a group with infinitely many group elements and also a differential manifold, meaning a space which locally look like the Euclidean space. Any group element can be written in terms of the group generator, T^a , and a number, θ^a , parametrizing the group element:

$$g = e^{i\theta^a T^a}. \quad (1.3)$$

The rule defining the Lie group is the Lie algebra (or Lie bracket), where the group generators must obey the following relation:

$$[T^a, T^b] = i f^{abc} T^c, \quad (1.4)$$

where repeated indices is summed over, by the Einstein summation convention, and f^{abc} is called the structure factor. The structure factor is antisymmetric under the permutation of its indices and depends on the group considered. For example, in

the case of the Pauli spin group, $SU(2)$, the group generators of the fundamental representation are the Pauli matrices, σ^a , conventionally normalized to $T^a = \frac{\sigma^a}{2}$. They satisfy $[T^a, T^b] = [\frac{1}{2}\sigma^a, \frac{1}{2}\sigma^b] = i\epsilon^{abc}\sigma^c$, and we can read off the structure factor as the Levi-Civita tensor, ϵ^{abc} .

Eq.(1.4) looks very similar to a commutation relation. The formal definition of the Lie bracket does not require that $[A, B] = AB - BA$, as long as the Jacobi identity holds. However, for most physical cases, where the theory is described by a group $SU(N)$, the generators are embedded into finite dimensional matrices, so the Lie bracket can be defined as a commutator. In terms of the structure factor, the Jacobi identity takes the form:

$$\begin{aligned} [T^a, [T^b, T^c]] + [T^b, [T^c, T^a]] + [T^c, [T^a, T^b]] &= 0 \\ [T^a, if^{bcd}T^d] + [T^b, if^{cad}T^d] + [T^c, if^{abd}T^d] &= 0 \\ if^{bcd}if^{ade}T^e + if^{cad}if^{bde}T^e + if^{abd}if^{cde}T^e &= 0 \\ f^{bcd}f^{ade} + f^{cad}f^{bde} + f^{abd}f^{cde} &= 0. \end{aligned}$$

A Lie group is said to be Abelian, after the Norwegian mathematician Niels Henrik Abel, if $f^{abc} = 0$, i.e. if the generators commute. Otherwise, the group is said to be non-Abelian.

Representations and the Casimir, C_R

In particle physics, the two most important representations of a group are the fundamental representation (F) and the adjoint representation (A or adj). The fundamental representation is the smallest non-trivial representation of the algebra [3, p.484]. In $SU(N)$, the fundamental representation is built up by $N \times N$ traceless, hermitean matrices with determinant 1. In $SU(2)$, this was the 2×2 matrices $T_F^a = \sigma^a/2$ where the subscript, F , refers to the fundamental representation. Using Eq.(1.1), we can check that these conditions are fulfilled:

$$\text{Tr}[\sigma^1] = \text{Tr} \begin{pmatrix} 0 & 1 \\ 1 & 0 \end{pmatrix} = 0 \quad \rightarrow \text{Traceless}, \quad (1.5)$$

$$(\sigma^1)^\dagger = \begin{pmatrix} 0 & 1 \\ 1 & 0 \end{pmatrix}^\dagger = \begin{pmatrix} 0 & 1 \\ 1 & 0 \end{pmatrix} = \sigma^1 \quad \rightarrow \text{Hermitian}, \quad (1.6)$$

$$\det[\sigma^1] = \begin{vmatrix} 0 & 1 \\ 1 & 0 \end{vmatrix} = 0 - (-1) = 1, \quad (1.7)$$

which can easily be shown for σ^2 and σ^3 as well.

In SU(3), the fundamental representation is a 3×3 matrix, $(T_F^a)_{ij}$, where the position in the matrix, (ij) , denotes the colour. There are three colours, such that $i =$ red, blue or green.

The adjoint representation is defined by the structure factor of the group considered:

$$(T_{adj}^a)^{bc} = -if^{abc}. \quad (1.8)$$

The adjoint representation acts on the vector space spanned by the generators. There are $N^2 - 1$ generators embedded into matrices for the group SU(N). Since there are $N^2 - 1$ generators, the adjoint representation must consist of $N^2 - 1$ dimensional matrices. In SU(2), the structure factor was the Levi-Civita tensor. The dimension of the adjoint representation is $N^2 - 1 = 2^2 - 1 = 3$, thus we must use the 3-dimensional Levi-Civita tensor which takes the form:

$$\epsilon^{abc} \begin{cases} +1 & , \text{ for even permutations } (abc) : (123), (231), (312) \\ -1 & , \text{ for odd permutations } (abc) : (321), (213), (132) \\ 0 & , \text{ for any repeated index.} \end{cases} \quad (1.9)$$

The Levi-civita tensor in 3 dimensions is a $3 \times 3 \times 3$ matrix. By assigning the 3 possible values for one of the indices, we can find the corresponding 2-dimensional 3×3 matrix of each "layer":

$$\epsilon^{1bc} = \begin{pmatrix} 0 & & \\ & 0 & 1 \\ & -1 & 0 \end{pmatrix}, \epsilon^{2bc} = \begin{pmatrix} 0 & -1 & \\ & 0 & \\ 1 & & 0 \end{pmatrix}, \epsilon^{3bc} = \begin{pmatrix} 0 & 1 & \\ -1 & 0 & \\ & & 0 \end{pmatrix}. \quad (1.10)$$

Combining Eq.(1.8) and Eq.(1.9), the adjoint representation of SU(2), T_{adj}^a , is given by

$$T_{adj}^1 = \begin{pmatrix} 0 & & \\ & 0 & -i \\ & i & 0 \end{pmatrix}, T_{adj}^2 = \begin{pmatrix} 0 & & i \\ & 0 & \\ -i & & 0 \end{pmatrix}, T_{adj}^3 = \begin{pmatrix} 0 & -i & \\ i & 0 & \\ & & 0 \end{pmatrix}. \quad (1.11)$$

For simplicity, only T_{adj}^a in SU(2) is derived since, in SU(3), the adjoint representations are 8×8 matrices.

The quadratic Casimir is defined as:

$$T_R^a T_R^a = C_R \mathbb{1}, \quad (1.12)$$

where the subscript R is denoting the representation considered, F (fundamental) or $A = adj$ (adjoint). It is some number produced by summing the square of the representation matrices of a group. Thus, it depends on both the group considered as well as the representation. An example is given for the fundamental representation in the group $SU(2)$. Recall that the generators in this group are the Pauli matrices. Casimir of the fundamental representation, C_F , in $SU(2)$ is found using Eq.(1.12) and Eq.(1.1). We get

$$\begin{aligned}
T_F^a T_F^a &= T_F^1 T_F^1 + T_F^2 T_F^2 + T_F^3 T_F^3 \\
&= \frac{\sigma^1 \sigma^1}{2 \ 2} + \frac{\sigma^2 \sigma^2}{2 \ 2} + \frac{\sigma^3 \sigma^3}{2 \ 2} \\
&= \frac{1}{4} \left[\begin{pmatrix} 0 & 1 \\ 1 & 0 \end{pmatrix} \begin{pmatrix} 0 & 1 \\ 1 & 0 \end{pmatrix} + \begin{pmatrix} 0 & -i \\ i & 0 \end{pmatrix} \begin{pmatrix} 0 & -i \\ i & 0 \end{pmatrix} + \begin{pmatrix} 1 & 0 \\ 0 & -1 \end{pmatrix} \begin{pmatrix} 1 & 0 \\ 0 & -1 \end{pmatrix} \right] \\
&= \frac{1}{4} \left[\begin{pmatrix} 1 & 0 \\ 0 & 1 \end{pmatrix} + \begin{pmatrix} 1 & 0 \\ 0 & 1 \end{pmatrix} + \begin{pmatrix} 1 & 0 \\ 0 & 1 \end{pmatrix} \right] \\
&= \frac{3}{4} \mathbb{1}.
\end{aligned} \tag{1.13}$$

Thus, $C_F = 3/4$ for $SU(2)$.

An easier way to find the Casimir for different representations in $SU(N)$ is given by the general formulas [1, p. 488]

$$C_F = \frac{N^2 - 1}{2N}, \quad C_A = N. \tag{1.14}$$

From this, the determination of the Casimirs of the group $SU(3)$ is straight forward. Since quantum chromodynamics is described by this group, we can note that the Casimirs of the fundamental and adjoint representations in $SU(3)$ are $C_F = \frac{3^2-1}{2 \cdot 3} = \frac{4}{3}$ and $C_A = 3$, respectively.

1.2 Theory of the strong interaction

Quantum chromodynamics is the quantum theory of strong interactions. The strong interaction is a short-ranged force and governs the nuclear interactions involving quarks and gluons. These are some of the elementary particles of the Standard Model. QCD is described by the symmetry group $SU(3)$ and is a non-Abelian gauge theory, i.e. $f^{abc} \neq 0$. The generators of this group are commonly written in terms of

normalized Gell-Mann matrices $T_F^a = \frac{1}{2}\lambda^a$, where the Gell-Mann matrices are given by Eq.(1.2).

In quantum electrodynamics, the theory describing charged particles interacting with the electric field, the force carriers (photons) only interact with electrically charged particles. The colour charge of a particle is a property related to strong interactions in QCD (from chromo: colour). In the Standard model, these particles are the quarks and gluons. Recall from the previous section that the position in the fundamental representation matrix, $(T_F^a)_{ij}$, denotes the colour ($i = 1, 2, 3 = \text{red, blue, green}$). Every particle has a corresponding antiparticle with the same mass and spin, but with the opposite electric charge and anticolour. E.g. the antiparticle corresponding to an up quark with colour red, will be the up antiquark with colour antired.

Figure 1.1 shows a table of the elementary particles in the Standard Model. The particles involved in QCD are the quarks and gluons, since these are the ones that carry colour charge. The quarks are the matter particles, and the gluons are the force carriers of the strong force. Due to the fact that gluons also carry a colour charge, the force carriers of QCD can interact with themselves (in contrast to QED where the photons cannot). The gluon propagator and the additional Feynman diagrams for the allowed interactions between gluons in QCD are derived in section 2.4.

Standard Model of Elementary Particles

three generations of matter (fermions)			interactions / force carriers (bosons)		
	I	II	III		
mass	$\approx 2.2 \text{ MeV}/c^2$	$\approx 1.28 \text{ GeV}/c^2$	$\approx 173.1 \text{ GeV}/c^2$	0	$\approx 124.97 \text{ GeV}/c^2$
charge	$\frac{2}{3}$	$\frac{2}{3}$	$\frac{2}{3}$	0	0
spin	$\frac{1}{2}$	$\frac{1}{2}$	$\frac{1}{2}$	1	0
	u up	c charm	t top	g gluon	H higgs
QUARKS	d down	s strange	b bottom	γ photon	
	$\approx 4.7 \text{ MeV}/c^2$	$\approx 96 \text{ MeV}/c^2$	$\approx 4.18 \text{ GeV}/c^2$	0	
	$-\frac{1}{3}$	$-\frac{1}{3}$	$-\frac{1}{3}$	0	
	$\frac{1}{2}$	$\frac{1}{2}$	$\frac{1}{2}$	1	
	e electron	μ muon	τ tau	Z Z boson	
LEPTONS	$\approx 0.511 \text{ MeV}/c^2$	$\approx 105.66 \text{ MeV}/c^2$	$\approx 1.7768 \text{ GeV}/c^2$	$\approx 91.19 \text{ GeV}/c^2$	
	-1	-1	-1	0	
	$\frac{1}{2}$	$\frac{1}{2}$	$\frac{1}{2}$	1	
	ν_e electron neutrino	ν_μ muon neutrino	ν_τ tau neutrino	W W boson	
	$< 1.0 \text{ eV}/c^2$	$< 0.17 \text{ MeV}/c^2$	$< 18.2 \text{ MeV}/c^2$	$\approx 80.39 \text{ GeV}/c^2$	
	0	0	0	± 1	
	$\frac{1}{2}$	$\frac{1}{2}$	$\frac{1}{2}$	1	
				GAUGE BOSONS VECTOR BOSONS	SCALAR BOSONS

Figure 1.1: Standard model of elementary particles [4].

Confinement

Gluon-gluon interactions are believed to give rise to colour confinement. At large separation distance, the potential between two quarks is thought to increase linearly, that is, $V_{\text{QCD}}(r) \sim kr$, for some constant, k [5]. At small separation distance, the potential between two quarks will be given by the Coulomb potential, $V_{\text{Coulomb}}(r) = -\frac{4}{3} \frac{g^2}{4\pi r} = -\frac{4}{3} \frac{\alpha}{r}$, where the strong coupling constant is defined as $\alpha = g^2/4\pi$. This potential will be derived on page 22.

Figure 1.2 shows the overall QCD potential, $V_{\text{QCD}}(r) = -\frac{4}{3} \frac{\alpha}{r} + kr$. For simplicity, α have been factored out, and the value of $k/\alpha = 3$ have been used to sketch the potential.

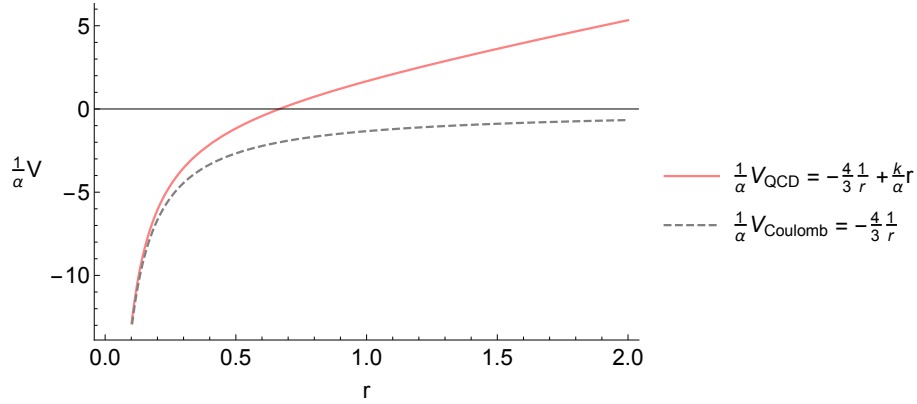


Figure 1.2: Potential as a function of distance between quarks. The overall QCD potential is $V_{\text{QCD}}(r) = -\frac{4}{3} \frac{\alpha}{r} + kr$. The Coulomb potential, $V_{\text{Coulomb}}(r) = -\frac{4}{3} \frac{\alpha}{r}$, is also shown. The coupling constant, α , has been factored out so the only α -depending term left is the linear term, $\frac{k}{\alpha}r$, of $\frac{1}{\alpha}V_{\text{QCD}}$. In this sketch, the value of $k/\alpha = 3$ have been used. At large distances, the strength of the force between a quark-antiquark pair increases linearly, and is why we do not observe isolated quarks. This plot is motivated by [5].

The strong interaction forces the quarks to be bound into colour-neutral states, called hadrons. Trying to separate two quarks by stretching them far apart will, due to the increasing potential, create a quark-antiquark pair instead of separating them (see Figure 1.3 for illustration). This is why one cannot see isolated quarks in nature and is what we call confinement. We can think of the strong force as a thick rubber band. Trying to separate two quarks by pulling them apart will only increase the strength

of the force between them. The strong force acting between two quarks increases with the distance separating them.

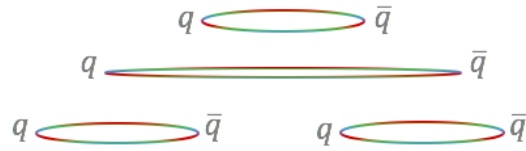


Figure 1.3: Illustration of the strong force carried by gluons between quarks.

There are two main types of hadrons called mesons and baryons. Mesons are built up by a quark and an antiquark ($q\bar{q}$) which have the same colour, e.g. red and antired, making them a colour-neutral combination. We can also have three quarks or antiquarks (qqq or $\bar{q}\bar{q}\bar{q}$) each carrying a different colour (red, blue or green). These are called baryons. Two of the best known baryons are the proton (uud) and the neutron (udd), which are the building blocks of atomic nuclei. Any colour-neutral combination containing a higher number of quarks and antiquarks, are called exotic hadrons. Examples of these are the tetraquark ($qq\bar{q}\bar{q}$), made of two mesons, and the pentaquark ($qqqq\bar{q}$), which is a combination of a meson and a baryon. ¹.

Asymptotic freedom and deconfinement

The running of the coupling constant, α , refers to the fact that the coupling constant depends on the energies involved. For low energies (large distances), the coupling constant is very large, and decreases with increasing energies (small distances). The property that the interaction strength, or the coupling constant, between quarks becomes weaker with decreasing distance is called asymptotic freedom.

1.3 Quark-Gluon Plasma

In ordinary matter, quarks are confined into hadrons. In quark-gluon plasma, the quarks are deconfined due to high temperatures and pressure. Inside this high energy-density region, quarks are moving freely without being coupled into hadrons. QGP

¹Recent discovery of previously predicted exotic hadrons, which consists of a higher number of quarks and antiquarks, have been observed at LHC at CERN. From 2003 there have been proposed several candidates for observation of these exotic hadrons. In 2015 LHCb reported the pentaquark $uud\bar{c}$ [6] and in 2020 they announced the discovery of the tetraquark $cc\bar{c}\bar{c}$ [7].

is a state of matter with approximately (local) thermal equilibrium. It is a nearly perfect fluid, which means that it can be described well using hydrodynamics. QGP filled the early universe. It is therefore of much interest to understand the properties of this state of matter. To create QGP one needs extreme temperatures and pressure beyond what can be found naturally on Earth today. By accelerating heavy-ions, like is done at the Relativistic Heavy Ion Collider (RHIC) at Brookhaven National Laboratory and at the Large Hadron Collider (LHC) at CERN, the velocity of the nuclei is boosted up to velocities comparable with the speed of light ². Colliding two such nuclei will provide the high energy needed to create QGP. The plasma produced can then be studied by observation of the final states produced in the collisions.

One motivation for the study on heavy-ion collisions, is to learn more about the phase diagram of QCD. Fig. 1.4 shows the conjectured phase diagram for QCD in terms of temperature, T , and baryon chemical potential, μ_B . The baryon chemical potential can be thought of as the excess of matter to antimatter. Thus, at high μ_B , there is a higher amount of matter compared to antimatter. For small μ_B and low T , the quarks exist in a confined hadron gas. Increasing the temperature, a continuous crossover into quark-gluon plasma phase occurs. The region at large μ_B and low T is of importance for the study of different regions in neutron stars. Around this region of the diagram, there is hypothesized to be a first order transition between the hadron gas and the QGP [9] [10], illustrated by the solid line in Figure 1.4. Probing heavy-ion collisions at smaller μ_B and higher T , we can learn whether (and where) a critical point exist between the continuous and first-order transitions.

Observables supporting the creation of QGP in heavy-ion collisions are collective flow, parton energy-loss and strangeness enhancements, which will all be discussed in Section 3.2.1. By comparing data with a proton-proton (pp) collision, where no medium is formed, we clearly see that in heavy-ion (AA) collisions, something is interacting with the particles involved. This suggests the formation of QGP in the latter case. A study of how particles are affected by a medium created in AA-collisions is done in Chapter 4.

²As an estimate using the collision energies available at LHC, the relativistic gamma-factors corresponds to 1400 [8], producing velocities of $v_z = 1/\sqrt{1 - \gamma^{-2}} = 1/\sqrt{1 - 1400^{-2}} = 0.9999$ (units in c).

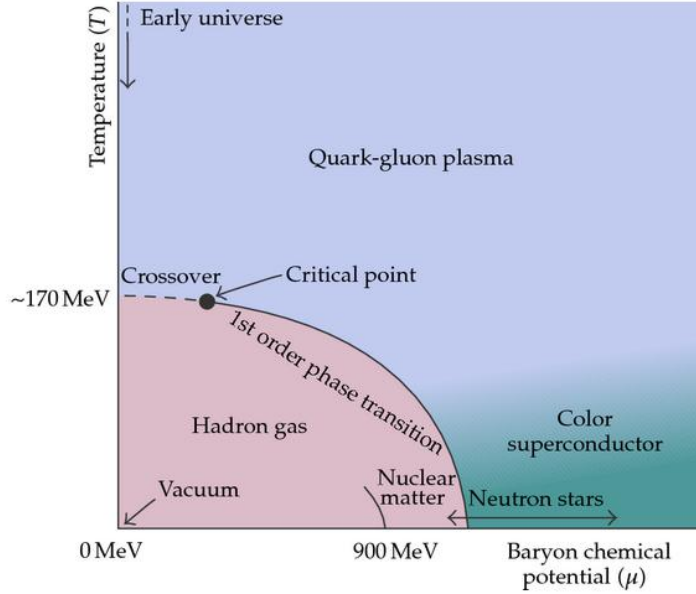


Figure 1.4: This figure shows the conjectured phase diagram for QCD. There is a continuous crossover from the hadron gas phase to the quark-gluon phase at low μ_B and T . If there is a 1st order phase transition occurring around $T \sim 170$ MeV and $\mu_B < 900$ MeV is only suggested. By probing heavy-ion collisions, one might determine whether there is a critical value for which the continuous crossover turns into a 1st order phase transition occurs. Figure from [11].

1.4 Perfect fluid

Shear viscosity, η , is a measure of the internal friction in a fluid. The dimensionless ratio, η/s (viscosity/entropy), is used to determine how “perfect” a fluid is. The lower bound conjectured to this ratio is $\eta/s \geq 1/4\pi \approx 0.08$ [12]. Meaning that if we have a fluid with $\eta/s = 1/4\pi$, we have a perfect fluid which can then be described approximately by hydrodynamics. Figure 1.5 shows constant pressure curves for η/s vs. temperature for different fluids. At the critical temperature, T_0 , a phase transition from a gaseous phase (left hand side of T_0) to a liquid phase (right hand side of T_0) occurs. For gases, the ratio decrease with temperature, and for liquids it increases. We see that for QGP, this ratio is almost at the boundary conjectured, $\eta/s = 1/4\pi$, implying that this is a nearly perfect fluid.

However, this lower bound have since been argued to be $\eta/s \geq 16/251/4\pi \approx 0.05$ [14]

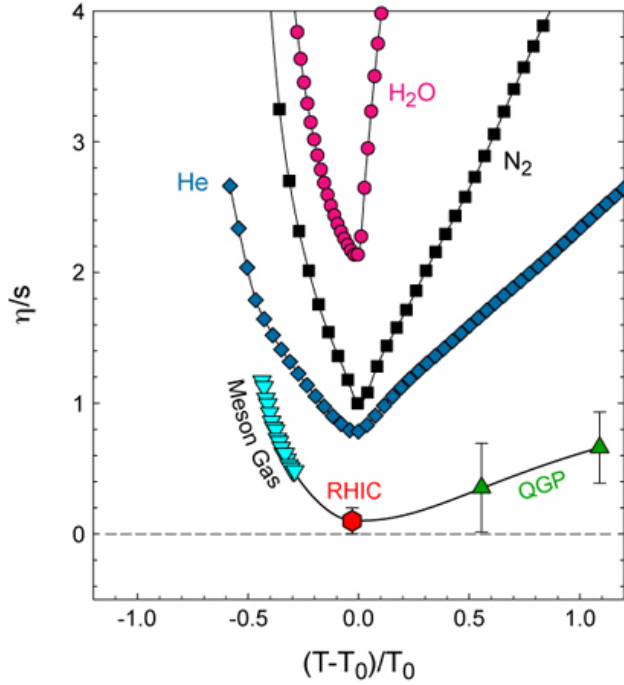


Figure 1.5: Constant pressure curves for different fluids/gases. T_0 is the critical temperature for the phase transition. Gaseous phases to the left and liquid phases to the right side of the plot. The ratio approaches the value of $\eta/s \approx 1/4\pi$, conjectured by [12] Figure from [13].

and also, from a quantum field theory point of view, that the ratio should approach 0 [15]. When applying the most complete Bayesian fits nowadays, the ratio fitted to the data from LHC experiments also show a lower value than $\eta/s < 1/4\pi$ [16]. Even though the lowest possible value of η/s is yet to be determined, QGP is still the most perfect fluid discovered so far.

Chapter 2

QCD: Derivations

In this chapter, some results of QCD are derived. These are based on the theory given in [3, ch.25+26] and [17, ch.15+16]. In Section 2.1, the action in the lattice is connected to that of the Yang-Mills theory using a plaquette, which is the smallest loop one can make on the lattice. In Section 2.2, the gluon propagator is derived. A short study of the interaction between quarks is given in Section 2.3. Lastly, the derivation of the Feynmann diagrams for the three- and four-point gluon vertices are presented in Section 2.4.

2.1 Action on the lattice

This derivation closely follows [3, p.504-505]. We want to compare field values at different point in our lattice in a gauge invariant way. The field values transforms as

$$\phi(n) \rightarrow e^{i\alpha^a(n)T^a} \phi(n) = U(n) \phi(n) \tag{2.1}$$

$$\phi^+(n) \rightarrow \phi^+(n) U^+(n), \tag{2.2}$$

where $\alpha^a(n)$ are real functions of space-time and T^a are the group generators of the fundamental representation in SU(3).

Since the convention used at a point x^μ should be independent of the convention used at a different point, y^μ , the difference between them would be phase-dependent. To be able to compare the field values independent of the phase used, we create a new field, W_μ , that acts as a link between two sites. If the sites are separated by a

distance a , $\hat{\mu}$ has the unit length a in μ -direction and $(n+\hat{\mu})$ and (n) are neighbouring sites (see Figure 2.1). The new field transforms as

$$W_\mu(n) \rightarrow U(n) W_\mu(n) U^\dagger(n + \hat{\mu}). \quad (2.3)$$

The fields, $W_\mu(n_i)$, are called link fields. We define $W_{-\mu}(n) = W_\mu^\dagger(n - \hat{\mu})$ as the link in the opposite direction. In the continuum case: $W_\mu(n) = e^{iaA_\mu^a(n)T^a} = e^{ia\mathbf{A}_\mu}$. The simplest loop one can make that is non-trivial is a small box called a plaquette:

$$\begin{aligned} W_{\mu\nu}(n) &= W_{-\nu}(n + \hat{\nu}) W_{-\mu}(n + \hat{\mu} + \hat{\nu}) W_\nu(n + \hat{\mu}) W_\mu(n) \\ &= W_\nu^+(n + \hat{\nu} - \hat{\nu}) W_\mu^+(n + \hat{\mu} + \hat{\nu} - \hat{\mu}) W_\nu(n + \hat{\mu}) W_\mu(n) \\ &= W_\nu^+(n) W_\mu^+(n + \hat{\nu}) W_\nu(n + \hat{\mu}) W_\mu(n). \end{aligned} \quad (2.4)$$

A plaquette is the multiplication of link-fields around a closed loop, and is a gauge invariant object.

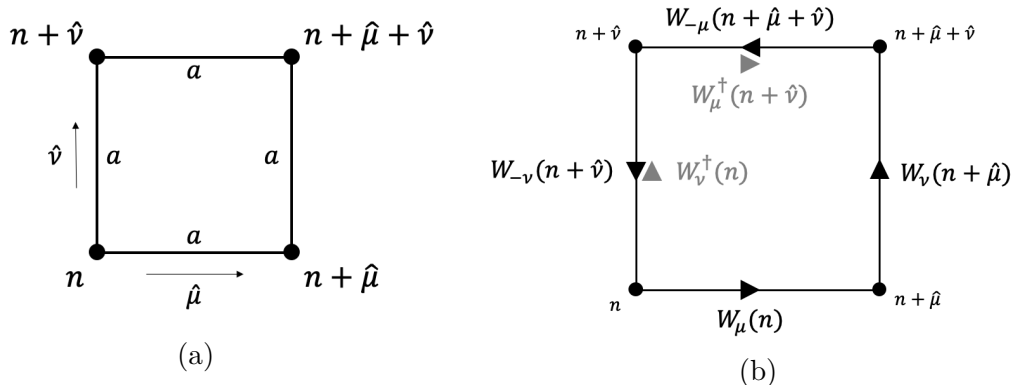


Figure 2.1: (a) Neighbouring sites on a lattice. Each site is separated by a distance, a , in either $\hat{\mu}$ -direction or $\hat{\nu}$ -direction, where $|\hat{\mu}| = |\hat{\nu}| = a$. (b) The smallest, non-trivial loop one can make on the lattice is called a plaquette. The link fields, $W_\mu(n)$, compare the field values of two neighbouring sites. The two gray arrows denotes the corresponding link fields in the opposite direction, as used in Eq.(2.4). Figure inspired by [3, p. 504].

Using the Campbell-Baker-Hausdorff formula, $\exp(A)\exp(B) = \exp(A+B+\frac{1}{2}[A,B])$, where $[A, B]$ is the commutation relation between A and B , one can write $W_{\mu\nu}$ up

to order a^2

$$\begin{aligned}
W_{\mu\nu}(n) = \exp \Big\{ & ia \left(-\mathbf{A}_\nu(n) - \mathbf{A}_\mu(n + \hat{\nu}) + \mathbf{A}_\nu(n + \hat{\mu}) + \mathbf{A}_\mu(n) \right) \\
& + \frac{1}{2}(-ia)^2 [\mathbf{A}_\nu(n), \mathbf{A}_\mu(n + \hat{\nu})] + \frac{1}{2}(ia)^2 [\mathbf{A}_\nu(n + \hat{\mu}), \mathbf{A}_\mu(n)] \\
& + \frac{1}{2}(-ia)(ia) [\mathbf{A}_\nu(n) + \mathbf{A}_\mu(n + \hat{\nu}), \mathbf{A}_\nu(n + \hat{\mu}) + \mathbf{A}_\mu(n)] \Big\}. \quad (2.5)
\end{aligned}$$

We Taylor-expand to connect to the continuum limit: $\mathbf{A}_\nu(n + \hat{\nu}) = \mathbf{A}_\nu(n) + a\partial_\mu \mathbf{A}_\nu(n) + \mathcal{O}(a^2)$.

$$\begin{aligned}
W_{\mu\nu} = \exp \Big\{ & ia \left(-\mathbf{A}_\nu(n) - \mathbf{A}_\mu(n) - a\partial_\nu \mathbf{A}_\mu(n) + \mathbf{A}_\nu(n) + a\partial_\mu \mathbf{A}_\nu(n) + \mathbf{A}_\mu(n) \right) \\
& - \frac{a^2}{2} [\mathbf{A}_\nu(n), \mathbf{A}_\mu(n) + a\partial_\nu \mathbf{A}_\mu(n)] - \frac{a^2}{2} [\mathbf{A}_\nu(n) + a\partial_\mu \mathbf{A}_\nu(n), \mathbf{A}_\mu(n)] \\
& + \frac{a^2}{2} [\mathbf{A}_\nu(n) + \mathbf{A}_\mu(n) + a\partial_\nu \mathbf{A}_\mu(n), \mathbf{A}_\nu(n) + \mathbf{A}_\mu(n) + a\partial_\mu \mathbf{A}_\nu(n)] \Big\}. \quad (2.6)
\end{aligned}$$

Up to order a^2 , the last term vanishes. We use that $[\mathbf{A}_\nu, \mathbf{A}_\mu] = -[\mathbf{A}_\mu, \mathbf{A}_\nu]$ and get

$$\begin{aligned}
W_{\mu\nu} &= \exp \Big\{ ia^2 \left(\partial_\mu \mathbf{A}_\nu(n) - \partial_\nu \mathbf{A}_\mu(n) \right) + a^2 [\mathbf{A}_\mu(n), \mathbf{A}_\nu(n)] + \mathcal{O}(a^3) \Big\} \\
&= \exp \Big\{ ia^2 \mathbf{F}_{\mu\nu}(n) + \mathcal{O}(a^3) \Big\}, \quad (2.7)
\end{aligned}$$

where the field-strength tensor is defined as $\mathbf{F}_{\mu\nu} \equiv (\partial_\mu \mathbf{A}_\nu - \partial_\nu \mathbf{A}_\mu) - i[\mathbf{A}_\mu, \mathbf{A}_\nu]$.

We want to relate the action on the lattice using the plaquette to that of the Yang-Mills action expressed in terms of the field-strength tensor. We can discretize the continuum of S_{YM} by rescaling $A_\mu \rightarrow \frac{1}{g} A_\mu$ and use that the index of the adjoint representation in a non-Abelian gauge theory is $T(\text{adj}) = C_A = N$:

$$S_{\text{YM}}[F_{\mu\nu}] = i \int d^4x \left[-\frac{1}{4g^2} (F_{\mu\nu}^a)^2 \right] = -\frac{ia^4}{4g^2 N} \Sigma_{n,\mu\nu} \text{tr}(\mathbf{F}_{\mu\nu}^2). \quad (2.8)$$

We then define the Yang-Mills action on the lattice to be

$$S_{\text{lattice}}[W_{\mu\nu}] = -\frac{i}{2g^2 N} \Sigma_{n,\mu\nu} \text{Re} \left[\text{tr}(1 - W_{\mu\nu}(N)) \right], \quad (2.9)$$

so that when we expand $W_{\mu\nu}$ at small a , we get

$$\begin{aligned} S_{\text{lattice}}[W_{\mu\nu}] &= -\frac{i}{2g^2N} \sum_{n,\mu\nu} \text{Re} \left[\text{tr} \left(1 - (1 + ia^2 \mathbf{F}_{\mu\nu}(N) - \frac{a^4}{2} \mathbf{F}_{\mu\nu}^2(N) + \mathcal{O}(a^5)) \right) \right] \\ &= -\frac{ia^4}{4g^2N} \sum_{n,\mu\nu} \text{tr}(\mathbf{F}_{\mu\nu}^2(N)), \end{aligned} \quad (2.10)$$

which is the same as the discrete version of the Yang-Mills action, Eq.(2.8).

2.2 The Gluon propagator

We can find the gluon propagator using the generating functional [3, p.262]

$$\langle \Omega | T \{ A_\mu(x_1) A_\nu(x_2) \} | \Omega \rangle = (-i)^2 \frac{1}{Z[0]} \frac{\partial^2 Z[J]}{\partial J_1 \partial J_2} \Big|_{J=0} = \Pi_{\mu\nu}(x_1 - x_2). \quad (2.11)$$

In our case, the functional $\mathcal{Z}[J] = \int \mathcal{D}A e^{iS[A] + i \int d^4x J(x) A(x)}$, without the presence of a source will be

$$\mathcal{Z}[0] = \int \mathcal{D}A e^{iS[A]} = \int \mathcal{D}A e^{i \int d^4x \left[-\frac{1}{4} (F_{\mu\nu}^a)^2 \right]} = \int \mathcal{D}A e^{i \int d^4x \left[-\frac{1}{2} A_\mu^a (\partial^2 g_{\mu\nu} - \partial_\mu \partial_\nu) \delta^{ab} A_\nu^b \right]}. \quad (2.12)$$

Given a vector \vec{p} with n dimensions, a Gaussian integral is related to the matrix of the quadratic part via the relation [3, p.255]

$$\int_{-\infty}^{\infty} d\vec{p} e^{-\frac{1}{2} \vec{p}^\dagger \mathbf{M} \vec{p} + \vec{J} \vec{p}} = \sqrt{\frac{(2\pi)^n}{\det \mathbf{M}}} e^{\frac{1}{2} \vec{J}^\dagger \mathbf{M}^{-1} \vec{J}}. \quad (2.13)$$

In momentum space, the matrix we are interested in from Eq.(2.12), namely $(\partial^2 g_{\mu\nu} - \partial_\mu \partial_\nu)$, will read: $(-k^2 g_{\mu\nu} + k_\mu k_\nu)$. For eigenvalues proportional to k_μ or k_ν , we will have $\det(-k^2 g_{\mu\nu} + k_\mu k_\nu) = 0$, which means that this matrix is not invertible. We will therefore follow the logic behind the the following idea: Suppose we have an integral of the form $\int dx dy e^{-x^2}$. This will not change if we shift y by some variable, say y' . We can therefore insert the delta-function $\int dy' \delta(y - y') = 1$ into the previous integral, without changing the total expression. We could also add a Gaussian which depends on y' , and divide by some normalization constant (\mathcal{N}) in front to make this

contribution 1. Thus we can write the initial integral as

$$\int dx dy e^{-x^2} = \mathcal{N} \int dx dy e^{-x^2} \int dy' e^{-\frac{(y')^2}{\sigma^2}} \delta(y - y') = \mathcal{N} \int dx dy e^{-x^2 - \frac{(y)^2}{\sigma^2}}. \quad (2.14)$$

The gauge field transforms in the non-Abelian theory as follows:

$$A_\mu^a \rightarrow A_\mu^a + \frac{1}{g} \partial_\mu \pi^a + f^{abc} A_\mu^b \pi^c = A_\mu^a + \frac{1}{g} D_\mu \pi^a = A^\pi, \quad (2.15)$$

where A^π denotes the transformed field and D_μ is the covariant derivative defined as $D_\mu = \partial_\mu + g f^{abc} A_\mu^a$.

Since the action should be invariant under this change, it should stay invariant under a shift in π^a as well. We have that $1 = \int dx \delta(ax) = \int du \frac{\delta(u)}{|a|}$. If \bar{x} is a n -dimensional vector, we can similarly write $1 = \int d\bar{x} \delta(a\bar{x}) = \int d\bar{u} \frac{\delta(\bar{u})}{|a|}$. If we now have a function of a vector as the argument in the delta-function, we get the Jacobian because of the change of variables, which gives us the relation

$$1 = \int d\bar{x} \delta(f(\bar{x})) = \int d\bar{u} \frac{\delta(\bar{u})}{\det|f'(\bar{x})|}. \quad (2.16)$$

We can rewrite this expression in terms of π^a , A^π and $G(A^\pi)$, which is some smooth function of the transformed field A_μ^a ,

$$1 = \int \mathcal{D}\pi \delta(G(A^\pi)) \det\left(\frac{\partial G(A^\pi)}{\partial \pi^a}\right), \quad (2.17)$$

where $\mathcal{D}\pi$ is the integral over all possible π .

Then we can write Eq.(2.12) as

$$\int \mathcal{D}A e^{iS[A]} = \int \mathcal{D}A e^{iS[A]} \int \mathcal{D}\pi \delta(G(A^\pi)) \det\left(\frac{\partial G(A^\pi)}{\partial \pi^a}\right). \quad (2.18)$$

We choose the generalized Lorentz gauge condition $G(A) = \partial_\mu A_\mu^a - w^a$, such that $G(A^\pi) = \partial_\mu A_\mu^a + \frac{1}{g} \partial_\mu D_\mu \pi^a - w^a$. The determinant can then be evaluated, and it turns out to be invariant of π^a , as claimed above.

$$\det\left(\frac{\partial G(A^\pi)}{\partial \pi^a}\right) = \det\left(\frac{\partial(\partial_\mu A_\mu^a + \frac{1}{g} \partial_\mu D_\mu \pi^a - w^a)}{\partial \pi^a}\right) = \frac{1}{g} \det(\partial_\mu D_\mu). \quad (2.19)$$

Since the determinant does not depend on π^a we can take it out of the π -integral. It does however depend on the covariant derivative, and thus the field A_μ^a , so we must still include it in the remaining integral over A . Inserting Eq.(2.19) into Eq.(2.18), we get

$$\int \mathcal{D}A e^{iS[A]} = \mathcal{N} \int \mathcal{D}\pi \int \mathcal{D}A e^{iS[A]} \delta(G(A^\pi)) \det(\partial_\mu D_\mu), \quad (2.20)$$

where \mathcal{N} is the collection of all constants and normalization factors that appear along the derivation. If we now transform the field $A_\mu^a \rightarrow A^\pi$ according to Eq.(2.15), the integration measure will not change since it is an integral over all possible fields, so $\mathcal{D}A = \mathcal{D}A^\pi$. Similarly, nothing will happen to the action, since the Lagrangian is invariant under this transformation, thus $S[A] = S[A^\pi]$. This means that we can think of A^π as a dummy-variable, and rename it to A . The delta-function can now be written in terms of the generalized gauge-condition, $G(A) = \partial_\mu A_\mu^a - w^a$. Let us follow the trick from Eq.(2.14) and add a Gaussian integral over w and put the corresponding normalization out in the front. Then we have,

$$\int \mathcal{D}A e^{iS[A]} = \mathcal{N} \int \mathcal{D}\pi \int \mathcal{D}A e^{iS[A]} \int \mathcal{D}w e^{-i \int d^4x \frac{1}{2\xi} (w^a)^2} \delta(\partial_\mu A_\mu^a - w^a) \det(\partial_\mu D_\mu), \quad (2.21)$$

where the factor of $\frac{1}{2\xi}$ is just a convention. We can write the determinant as a path integral over the Grassmann numbers, \bar{c} and c , in this way: $\det(\partial_\mu D_\mu) = \int \mathcal{D}\bar{c} \mathcal{D}c \exp[-i \int d^4x \bar{c} (\partial_\mu D_\mu) c]$ [3, p.497]. c and \bar{c} are called the Faddeev-Popov ghosts and anti-ghosts and are anticommuting Lorentz scalars. For each gauge field, A_μ , there is one ghost and one anti-ghost. Next, we use the delta-function to do the integral over w , which leave us at

$$\int \mathcal{D}A e^{iS[A]} = \mathcal{N} \int \mathcal{D}\pi \int \mathcal{D}A \mathcal{D}\bar{c} \mathcal{D}c e^{i \int d^4x \left[-\frac{1}{4} (F_{\mu\nu}^a)^2 - \frac{1}{2\xi} (\partial_\mu A_\mu^a)^2 - \bar{c} (\partial_\mu D_\mu) c \right]}. \quad (2.22)$$

Since we know that $S[A] = \int d^4x \mathcal{L}[A]$, we can read off the Lagrangian from this expression. We find the so-called Faddeev-Popov Lagrangian which is the gauge-fixed Lagrangian only involving the non-Abelian gauge-bosons:

$$\mathcal{L}_{R_\xi} = -\frac{1}{4} (F_{\mu\nu}^a)^2 - \frac{1}{2\xi} (\partial_\mu A_\mu^a)^2 - \bar{c} (\partial_\mu D_\mu) c = \mathcal{L}_{\text{Yang-Mills}} + \mathcal{L}_{\text{gauge fixing}} + \mathcal{L}_{\text{ghosts}}. \quad (2.23)$$

To find the gluon propagator, we need only look at the two first terms, since these are the ones containing two gauge-fields. Rearranging so that they can be written in

one term and switching to momentum space, we get

$$\begin{aligned}
-\frac{1}{4}(F_{\mu\nu}^a)^2 - \frac{1}{2\xi}(\partial_\mu A_\mu^a)^2 &= -\frac{1}{2}A_\mu^a\left(\partial^2 g_{\mu\nu} - \partial_\mu\partial_\nu + \frac{1}{\xi}\partial_\mu\partial_\nu\right)A_\nu^a \\
&= -\frac{1}{2}\int\frac{d^4k}{(2\pi)^4}A_\mu^a\left[-k^2g_{\mu\nu} + \left(1 - \frac{1}{\xi}\right)k_\mu k_\nu\right]A_\nu^a. \quad (2.24)
\end{aligned}$$

We invert the term in the bracket, which is acting as the matrix \mathbf{M} in Eq.(2.13). We must have that

$$\left[-k^2g_{\mu\sigma} + \left(1 - \frac{1}{\xi}\right)k_\mu k_\sigma\right]\Pi^{\sigma\nu} = g_\mu^\nu, \quad (2.25)$$

so we make an ansatz that $\Pi^{\sigma\nu}$ must be of the form $Ag^{\sigma\nu} + Bk^\sigma k^\nu$ since these are the only combinations we can make out of g and k . We use the identity that $g_{\mu\sigma}g^{\sigma\nu} = g_\mu^\nu$ and $g_{\mu\sigma}k^\sigma = k_\mu$. Then,

$$\left[-k^2g_{\mu\sigma} + \left(1 - \frac{1}{\xi}\right)k_\mu k_\sigma\right]\left[Ag^{\sigma\nu} + Bk^\sigma k^\nu\right] = g_\mu^\nu \quad (2.26)$$

$$-k^2Ag_\mu^\nu - k^2Bk_\mu k^\nu + \left(1 - \frac{1}{\xi}\right)Ak_\mu k^\nu + \left(1 - \frac{1}{\xi}\right)Bk_\mu k^2 k^\nu = g_\mu^\nu, \quad (2.27)$$

which give us two equations that we can solve for A and B:

$$\begin{aligned}
I : -k^2A &= 1 & \rightarrow A &= -\frac{1}{k^2}, \\
II : -k^2B + \left(1 - \frac{1}{\xi}\right)A + \left(1 - \frac{1}{\xi}\right)Bk^2 &= 0 & \rightarrow B &= \frac{1}{k^4}(1 - \xi).
\end{aligned}$$

We plug these values for A and B into our ansatz for $\Pi_{\mu\nu}$, and we arrive at the gluon propagator

$$i\Pi_{\mu\nu}^{ab} = \frac{-i}{k^2}\left[g_{\mu\nu} - \left(1 - \xi\right)\frac{k_\mu k_\nu}{k^2}\right]\delta^{ab}, \quad (2.28)$$

where the δ^{ab} comes from the colour of the fields. This propagator only differs from that of the photon propagator by the additional factor of δ^{ab} .

2.3 Attractive and repulsive interactions

We want to know if the interactions between a quark and an antiquark is attractive or repulsive. We can consider the $2 \rightarrow 2$ scattering process $u\bar{d} \rightarrow u\bar{d}$, where u is an

$$T_{j1}^a T_{1l}^a = \frac{1}{2} \left(\delta_{jl} \delta_{11} - \frac{1}{3} \delta_{j1} \delta_{1l} \right) = \begin{bmatrix} \frac{1}{3} & 0 & 0 \\ 0 & \frac{1}{2} & 0 \\ 0 & 0 & \frac{1}{2} \end{bmatrix}. \quad (2.32)$$

If we start out with red-antired, the final state colours can remain the same, or it can change to either blue-antiblue or green-antigreen with a slightly bigger probability. Similarly for the other two possible initial states where we have a colour and its corresponding anti-colour. The colour factor is $T_{j2}^a T_{2l}^a = \text{diag}(\frac{1}{2}, \frac{1}{3}, \frac{1}{2})$ for blue-antiblue and $T_{j3}^a T_{3l}^a = \text{diag}(\frac{1}{2}, \frac{1}{2}, \frac{1}{3})$ for green-antigreen. Either way, the colour factor comes out with a positive number and the sign of the matrix element will be the same as for the $e^- p^+ \rightarrow e^- p^+$ process, so this is an attractive interaction.

For the second case, we look at two different initial colour charges, e.g. red ($i = 1$) and antigreen ($k = 3$). Using the Fierz identity again, we find the $T_{j1}^a T_{3l}^a$ factor to be

$$T_{j1}^a T_{3l}^a = \frac{1}{2} \left(\delta_{jl} \delta_{13} - \frac{1}{3} \delta_{j1} \delta_{3l} \right) = \begin{bmatrix} 0 & 0 & -\frac{1}{6} \\ 0 & 0 & 0 \\ 0 & 0 & 0 \end{bmatrix}. \quad (2.33)$$

The final states will have the same colour charges as the initial states, which is not surprising since the colour must be conserved. This will be the case for all $i \neq k$, thus the matrix element will have a negative sign independent of the initial colours. Thus, we see that these interactions are repulsive.

Using the obtained values for $T_{ji}^a T_{kl}^a$ in Eq.(2.30), we find the potentials for the different interactions

$$V = -\frac{4}{3} \frac{g^2}{4\pi r}, \quad (\text{colour singlet, same initial colour}) \quad (2.34)$$

$$V = \frac{1}{6} \frac{g^2}{4\pi r}. \quad (\text{colour octet, different initial colour}) \quad (2.35)$$

supporting the conclusion of the attractive interaction between $q\bar{q}$ with same initial colour, and the repulsive interaction between $q\bar{q}$ of different initial colour.

2.4 Feynman rules for the gluon vertices

The interaction-terms in the non-Abelian theory is given by [3, p.510]

$$\begin{aligned}
\mathcal{L}_{\text{int}} = & -gf^{abc}(\partial_\mu A_\nu^a)A_\mu^b A_\nu^c - \frac{1}{4}g^2(f^{eab}A_\mu^a A_\nu^b)(f^{ecd}A_\mu^c A_\nu^d) \\
& + gf^{abc}(\partial_\mu \bar{c}^a)A_\mu^b c^c + gA_\mu^a \bar{\psi}_i \gamma^\mu T_{ij}^a \psi_j \\
& + igA_\mu^a T_{ij}^a (\phi_i^* \partial_\mu \phi_j - \phi_j \partial_\mu \phi_i^*) + g^2 \phi_i^* A_\mu^a T_{ik}^a T_{kj}^b A_\mu^b \phi_j. \tag{2.36}
\end{aligned}$$

The first and second term is representing interactions between three and four gluons, respectively. The third term is the interaction between a gluon, a ghost and an anti-ghost, and the fourth term is the quark-antiquark-gluon vertex. The two last terms are representing interactions involving complex fields. In our convention, the Fourier-transform of $A(x)$ is

$$A_\mu^a(x) = \int \frac{d^4k}{(2\pi)^4} e^{ikx} A_\mu^a(k). \tag{2.37}$$

2.4.1 Triple-gluon vertex

We will now derive the Feynman rule to the triple-gluon vertex, and start by looking at the first term in Eq.(2.36)

$$iS_{3\text{-point interaction}} = -igf^{abc} \int d^4x (\partial_\mu A_\nu^a(x)) A_\mu^b(x) A_\nu^c(x). \tag{2.38}$$

We want to do our calculation in momentum-space so we Fourier-transform Eq.(2.38) according to Eq.(2.37) and relabel $A_\nu = A_\rho g^{\rho\nu}$.

$$iS = -igf^{abc} \int d^4x \left(\partial_\mu \int \frac{d^4p}{(2\pi)^4} e^{ipx} A_\nu^a(p) \right) \int \frac{d^4k}{(2\pi)^4} e^{ikx} A_\mu^b(k) \int \frac{d^4q}{(2\pi)^4} e^{iqx} A_\rho^c(q) g^{\rho\nu}. \tag{2.39}$$

The derivative only acts on the x -dependence which occurs in the exponential, keeping in mind that the dot-product contains indices, $p_\mu \cdot x^\mu$, this gives a factor of ip_μ .

Rearranging the terms we get

$$\begin{aligned}
iS &= g f^{abc} \int \frac{d^4 p}{(2\pi)^4} \int \frac{d^4 k}{(2\pi)^4} \int \frac{d^4 q}{(2\pi)^4} \int d^4 x e^{ix(p+k+q)} p_\mu A_\nu^a(p) A_\mu^b(k) A_\rho^c(q) g^{\rho\nu} \\
&= g f^{abc} \int \frac{d^4 p}{(2\pi)^4} \int \frac{d^4 k}{(2\pi)^4} \int \frac{d^4 q}{(2\pi)^4} (2\pi)^4 \delta^{(4)}(p+k+q) p_\mu A_\nu^a(p) A_\mu^b(k) A_\rho^c(q) g^{\rho\nu} \\
&= g f^{abc} \int_{pkq} p_\mu A_\nu^a(p) A_\mu^b(k) A_\rho^c(q) g^{\rho\nu}, \tag{2.40}
\end{aligned}$$

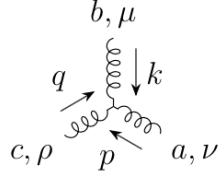
where we have defined \int_{pkq} to be all the integral terms and the delta-function term comes from the integral over x . This diagram is not symmetric, so we continue by making it symmetric around two of the axes by dividing the equation into two equal parts, and relabel the dummy-indices of one of them: $(a, \nu, p) \rightarrow (c, \rho, q)$.

$$\begin{aligned}
iS &= g \left[\frac{1}{2} \int_{pkq} f^{abc} p_\mu A_\nu^a(p) A_\mu^b(k) A_\rho^c(q) g^{\rho\nu} + \frac{1}{2} \int_{pkq} f^{abc} p_\mu A_\nu^a(p) A_\mu^b(k) A_\rho^c(q) g^{\rho\nu} \right] \\
&= \frac{g}{2} \left[\int_{pkq} f^{abc} p_\mu A_\nu^a(p) A_\mu^b(k) A_\rho^c(q) g^{\rho\nu} + \int_{qkp} f^{cba} q_\mu A_\rho^c(q) A_\mu^b(k) A_\nu^a(p) g^{\nu\rho} \right] \\
&= \frac{g}{2} \int_{pkq} f^{abc} A_\nu^a(p) A_\mu^b(k) A_\rho^c(q) g^{\rho\nu} (p_\mu - q_\mu), \tag{2.41}
\end{aligned}$$

where we have used the antisymmetry of f^{abc} in the last step. We do this one more time, making the diagram symmetric around all the axis by dividing into 3 parts (together with the 1/2 from above we get an overall factor of 1/3!). We permute the indices $(\nu, a, p) \rightarrow (\mu, b, k) \rightarrow (\rho, c, q)$ in one of the parts and then the other way around for the last one. We get

$$\begin{aligned}
iS &= \frac{g}{3!} \left[\int_{pkq} f^{abc} A_\nu^a(p) A_\mu^b(k) A_\rho^c(q) g^{\rho\nu} (p_\mu - q_\mu) \right. \\
&\quad + \int_{kqp} f^{bca} A_\mu^b(k) A_\rho^c(q) A_\nu^a(p) g^{\nu\mu} (k_\rho - p_\rho) \\
&\quad \left. + \int_{qpk} f^{cab} A_\rho^c(q) A_\nu^a(p) A_\mu^b(k) g^{\mu\rho} (q_\nu - k_\nu) \right] \\
&= \frac{g}{3!} f^{abc} \int_{pkq} A_\nu^a(p) A_\mu^b(k) A_\rho^c(q) [g^{\rho\nu} (p_\mu - q_\mu) + g^{\nu\mu} (k_\rho - p_\rho) + g^{\mu\rho} (q_\nu - k_\nu)]. \tag{2.42}
\end{aligned}$$

Again, the antisymmetry of f^{abc} is used as well as we can write the integrals independent of the order of p, k and q (i.e. $\int_{pkq} = \int_{kqp} = \int_{qpk}$). We have then obtained the Feynman rule for the triple-gluon vertex:



$$= g f^{abc} [g^{\rho\nu}(p_\mu - q_\mu) + g^{\nu\mu}(k_\rho - p_\rho) + g^{\mu\rho}(q_\nu - k_\nu)]. \quad (2.43)$$

2.4.2 Four-gluon vertex

The corresponding Feynman rule for the four-point gluon vertex is found using the second term of Eq.(2.36), $-\frac{1}{4}g^2 f^{eab} A_\mu^a A_\nu^b f^{ecd} A_\mu^c A_\nu^d$. In the same fashion as the previous section, we will use the short-hand notation for the integrals which comes from the Fourier-transform and the delta-function as $\int_{\mu\nu\rho\sigma}$. In the case of the four-point vertex, we do not have any derivative, so we will not get an extra factor of momentum. We will write $A_\mu^c = A_\rho^c g_{\mu\rho}$ and $A_\nu^d = A_\sigma^d g_{\nu\sigma}$ to separate them from each other. Taking all the A 's in front, we can focus on the structure-factors, f^{eab} and f^{ecd} , and the g 's. The action for the 4-point interaction can then be written as

$$iS_{4\text{-point interaction}} = -\frac{ig^2}{4} \int_{\mu\nu\rho\sigma} A_\mu^a A_\nu^b A_\rho^c A_\sigma^d f^{eab} f^{ecd} g_{\mu\rho} g_{\nu\sigma}. \quad (2.44)$$

There are $4!$ ways of permuting the μ, ν, ρ, σ -indices, giving us a symmetry-factor of $\frac{1}{4!}$. For simplicity, we rename the set of indices like this: $(a, \mu) = 1$, $(b, \nu) = 2$, $(c, \rho) = 3$ and $(d, \sigma) = 4$. The possible ways we can permute the three last indices giving that the first index stays the same is: 1234, 1243, 1324, 1342, 1423, 1432. Only looking at the structure-factors and the g 's (which are the ones that will be changing) with these permutations gives us these six terms in the integral:

$$\begin{aligned} & f^{e12} f^{e34} g_{13} g_{24} + f^{e12} f^{e43} g_{14} g_{23} \\ & + f^{e13} f^{e24} g_{12} g_{34} + f^{e13} f^{e42} g_{14} g_{32} \\ & + f^{e14} f^{e23} g_{12} g_{43} + f^{e14} f^{e32} g_{13} g_{42}. \end{aligned} \quad (2.45)$$

Using the antisymmetry of the structure-factor, $f^{e12} = -f^{e21}$, we can write this in a more compact form:

$$\begin{aligned} & f^{e12} f^{e34} (g_{13} g_{24} - g_{14} g_{23}) \\ & + f^{e13} f^{e24} (g_{12} g_{34} - g_{14} g_{32}) \\ & + f^{e14} f^{e23} (g_{12} g_{43} - g_{13} g_{42}). \end{aligned} \quad (2.46)$$

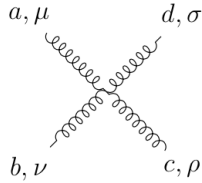
The next permutations will also give us six terms and are obtained by swapping two of the indices such that $(1234) \rightarrow (2134)$ in the previous expression. A cyclic shift to the right, $(1234) \rightarrow (4123)$, will also give us six terms. These $6 + 6$ terms are shown below:

$$\begin{aligned}
& f^{e21} f^{e34} (g_{23}g_{14} - g_{24}g_{13}) & f^{e41} f^{e23} (g_{42}g_{13} - g_{43}g_{12}) \\
& + f^{e23} f^{e14} (g_{21}g_{34} - g_{24}g_{31}) & + f^{e42} f^{e13} (g_{41}g_{23} - g_{43}g_{12}) \\
& + f^{e24} f^{e13} (g_{21}g_{43} - g_{23}g_{41}), & + f^{e43} f^{e12} (g_{41}g_{32} - g_{42}g_{31}). \tag{2.47}
\end{aligned}$$

After using the antisymmetry of the structure-factor and the symmetry of g ($g_{12} = g_{21}$), these terms turns out to be the same as those of Eq.(2.46). The last way of permuting is by swapping the two last indices and then do a cyclic shift to the right, i.e. $(1234) \rightarrow (1243) \rightarrow (3124)$. By using what we found out from the previous step, namely that if we swap two indices the terms will become that of Eq.(2.46) and similarly if we cyclically permute one step to the right, we know that these last six terms will also look exactly like Eq.(2.46). Then we are left with $4 \cdot$ Eq.(2.46), which cancels the $\frac{1}{4}$ in the front of Eq.(2.44), though we still have a factor of $\frac{1}{4!}$ from the symmetry mentioned above. Converting the indices back from numbers to letters, Eq.(2.44) now looks like

$$\begin{aligned}
iS_{4point} = -\frac{ig^2}{4!} \int_{\mu\nu\rho\sigma} A_\mu^a A_\nu^b A_\rho^c A_\sigma^d & \left[f^{eab} f^{ecd} (g_{\mu\rho}g_{\nu\sigma} - g_{\mu\sigma}g_{\nu\rho}) \right. \\
& + f^{eac} f^{ebd} (g_{\mu\nu}g_{\rho\sigma} - g_{\mu\sigma}g_{\rho\nu}) \\
& \left. + f^{ead} f^{ebc} (g_{\mu\nu}g_{\sigma\rho} - g_{\mu\rho}g_{\sigma\nu}) \right], \tag{2.48}
\end{aligned}$$

and we can read off the Feynman rule for the four-gluon vertex as:



$$\begin{aligned}
& = -ig^2 \left[f^{eab} f^{ecd} (g_{\mu\rho}g_{\nu\sigma} - g_{\mu\sigma}g_{\nu\rho}) \right. \\
& + f^{eac} f^{ebd} (g_{\mu\nu}g_{\rho\sigma} - g_{\mu\sigma}g_{\rho\nu}) \\
& \left. + f^{ead} f^{ebc} (g_{\mu\nu}g_{\sigma\rho} - g_{\mu\rho}g_{\sigma\nu}) \right]. \tag{2.49}
\end{aligned}$$

Chapter 3

Heavy-ion collisions

In heavy-ion (AA) collisions, nuclei are accelerated to relativistic velocities. The nucleus consists of protons and neutrons, which in turn are build up by quarks and gluons, collectively called partons. The mass number, A , is the sum of protons and neutrons in the nucleus. If the radius of the nucleus is R_A (e.g. $R_{\text{Pb}} \sim 15$ fm), the relativistic thickness is given by R_A / γ , where $\gamma = 1/\sqrt{1 - v_z^2}$ and v_z is the velocity of the nucleus in the direction of the beam in units of speed of light. For PbPb collisions at LHC, the nuclei are collided with a total collision energy $\sqrt{s} = 2.76$ TeV, giving us a gamma-factor of about $\gamma = 1400$. This means that the nuclei gets highly Lorentz contracted. Instead of thinking about two spheres colliding, we can imagine thin pancake-like objects. The impact parameter, b , is the distance between the center of the two nuclei. Observation of the centrality of a collision tries to tell us about the impact parameter. In a central collision, they collide head-on and thus $b = 0$. In a peripheral collision, $b \neq 0$, the collision will happen in the overlap region (see Fig. 3.1). The particles contributing in the collision process by colliding into other nucleons are called participants. Those not contributing are called spectators and will simply continue their paths along the beam axis.

3.1 Evolution of the collision

The physical picture of how the collisions are modelled is described in the following and illustrated in Figure 3.2. After about 1 fm/ c after the collision of the two Lorentz contracted nuclei, the quarks and gluons are deconfined into quark-gluon plasma. This state of matter is often described using relativistic hydrodynamics

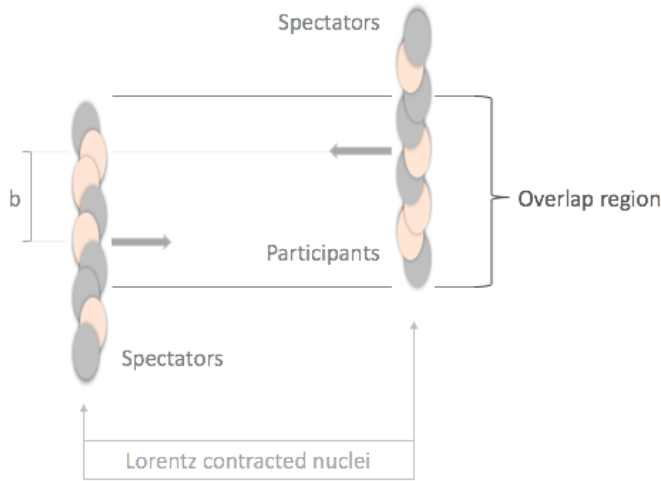


Figure 3.1: The participant nucleons in a collision of two Lorentz contracted disks are the ones inside the overlap region and collides with at least one other nucleon. The nucleons outside the overlap region are called the spectators. These will simply continue their paths along the beam axis. The impact parameter, b , tells how far the center of each nucleus is from each other. In a central (head-on) collision, $b = 0$.

since it is established as a strongly interacting fluid [18].

After expanding and consequently cooling for roughly $10 \text{ fm}/c$, quarks and gluons becomes confined into hadrons and resonances. This process is called hadronization. The hadrons continue to collide both inelastically, changing the species of the hadrons, and elastically, which alters their energy-momenta. Chemical freeze-out occurs when the inelastic scattering between hadrons stop. When the proper time between collisions are of the scales of the mean-free-path between the hadrons, i.e. $\tau_{coll} \sim \lambda_{mfp}$, kinetic freeze-out occurs and the elastic scattering stops. After $\sim 10\text{-}15 \text{ fm}/c$ the hadrons are free streaming to the detectors.

In a proton-proton (pp) collision, the participants will collide once and produce roughly 10 charged particles. In an AA-collision, the number of participating nucleons will be much higher and these will collide many times creating thousands of charged particles. E.g., AuAu-collisions taking place at RHIC happens with a total collision energy $\sqrt{s} = 200 \text{ GeV}$. About 5000 charged particles get created in these collisions [19], which is over 10 times the initial number of particles. In PbPb-collisions at LHC, the total collision energy is significantly higher, $\sqrt{s} = 2.76 \text{ TeV}$, so even more charged particles can be produced. In these large systems, QGP is formed due

to the multiple scatterings, high temperatures and enormous energies involved.

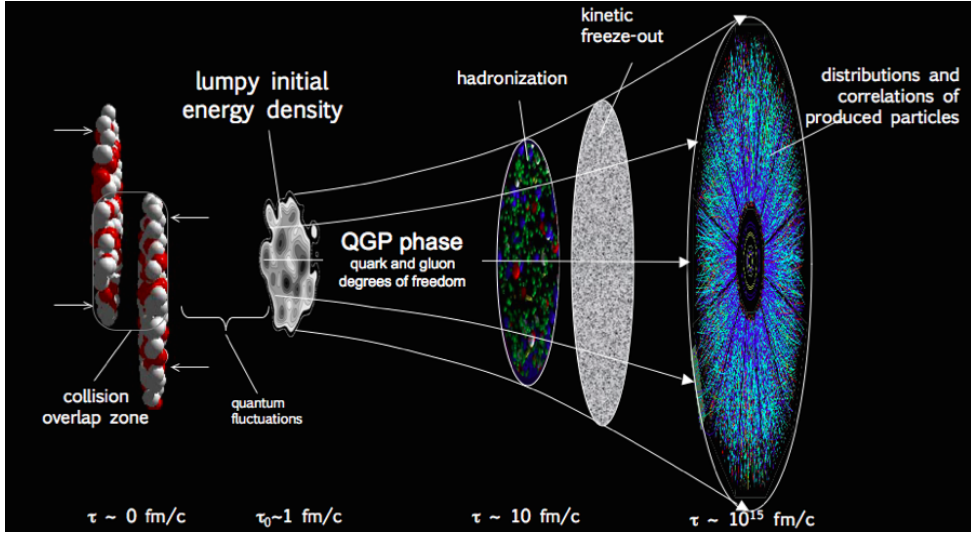


Figure 3.2: An illustration of the current understanding of how heavy-ion collisions evolve. Figure from [20].

3.2 Observables

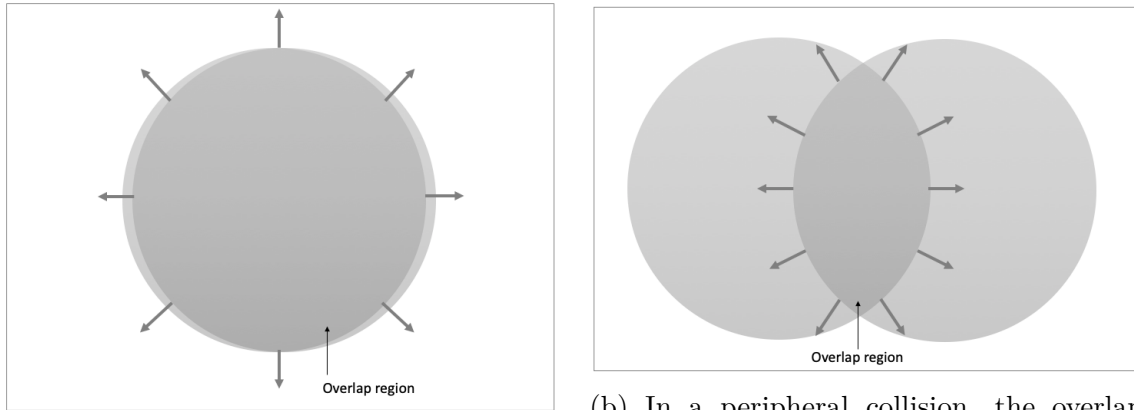
There are three important physical objects supporting the idea of the creation of QGP in heavy-ion collisions: collective flow, parton energy-loss and strangeness enhancement. The first is observed by the elliptic flow determined from anisotropies in the final states observables. The nuclear modification factor, R_{AA} , and jet-suppression are two observations for parton energy-loss. Strangeness enhancement in heavy-ion collisions shows a number of produced strange quarks comparable to predictions from thermal equilibrium, in contrast to what is observed in pp-collisions. In this section we will look closer at these four observables.

3.2.1 Elliptic flow

The initial momentum of the participants (the particles involved in the collision) will mostly be in the beam direction (longitudinal momentum, p_L). If any, they can also have some transverse momentum, p_T , which would be isotropically distributed. If the particles do not interact with each other after the collision, then the final transverse

momentum distribution will also be isotropic. If they instead interact with their surrounding particles with enough strength and frequency, the quarks can be deconfined within this small region, and achieve approximately (local) equilibrium.

The initial geometry of the overlap region can have an effect on the final momentum distribution. In a central collision, the two nuclei collide head-on and the initial geometry is (almost) circular (see Figure 3.3a). The pressure of the system will be distributed equally along the overlap region and it will expand isotropically in the radial direction. Thus, the final states observed will be equally distributed. In a peripheral collision of two Lorentz contracted discs, the overlap region will have e.g. an almond-like shape (see Figure 3.3b). Due to the spatial anisotropy in the medium, it will expand unevenly due to the difference in pressure. This will lead to anisotropy in the final momentum distribution.



(a) The overlap region in a central collision is nearly circular and is expanding equally in the radial direction.

(b) In a peripheral collision, the overlap region has an almond-like shape and will therefore have an anisotropic flow in the radial direction.

Figure 3.3: The geometry of the overlap region of collisions with different centrality is illustrated. The view is along the beam axis, i.e., either in or out of the paper.

Fig. 3.4 shows final energy distributions from four different collisions. In the upper left and bottom right corners, an almost circular distribution of the final states momentum is observed. Thus, these collisions are most likely central collisions. In the upper right and lower left corners of the figure, the final distributions shows a clear anisotropy in the final energies. This is an example of how the initial almond-like shape from Figure 3.3b have influenced the final states distribution.

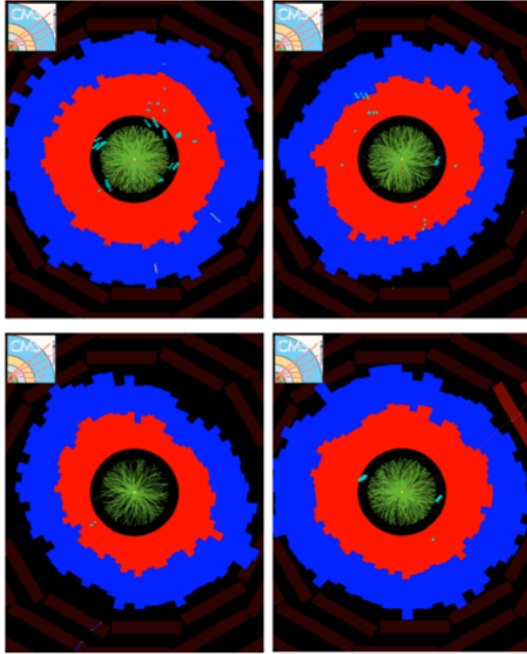


Figure 3.4: Azimuthal distribution measurements done by CMS. The charged particle tracks are shown in green. The red is the energy in the electromagnetic calorimeter, which is designed to measure the energies of particles interacting via the electromagnetic force (electrons, positrons, photons) [21]. The particles which interact via the strong force, i.e., colour charged particles, are measured using a hadronic calorimeter. By the time these particles hit the detector, they are confined into hadrons. Thus, the observed energies are from neutral hadrons and is shown in blue. A clear anisotropy in the final states are observed for the upper right and lower left corners. Figure from [8].

3.2.2 Nuclear modification factor, R_{AA}

The nuclear modification factor [22],

$$R_{AA}(p_T) = \frac{1}{\langle N_{coll} \rangle} \frac{dN^{AA}/dp_T}{dN^{pp}/dp_T}, \quad (3.1)$$

is a ratio between the number of particles produced in a AA-collision to the number produced in a similar pp-collision. The number of parton collisions in an AA-collision is denoted by $\langle N_{coll} \rangle$. A factor of this is included to normalize the AA-collision to that of a pp-collision.

The number of particles with momentum, p_T , produced in an AA-collision is given by dN^{AA}/dp_T . Similarly, the notation dN^{pp}/dp_T , represents the equivalent yield in a pp-collision. If no medium were produced in the AA-collision, we would expect that $R_{AA} \approx 1$, i.e., that the number of particles with momentum, p_T , produced were roughly the same. However, if there is a medium present in the collision, the momentum of the produced particles may be affected due to interactions with the medium. Thus, we will expect that $R_{AA} < 1$.

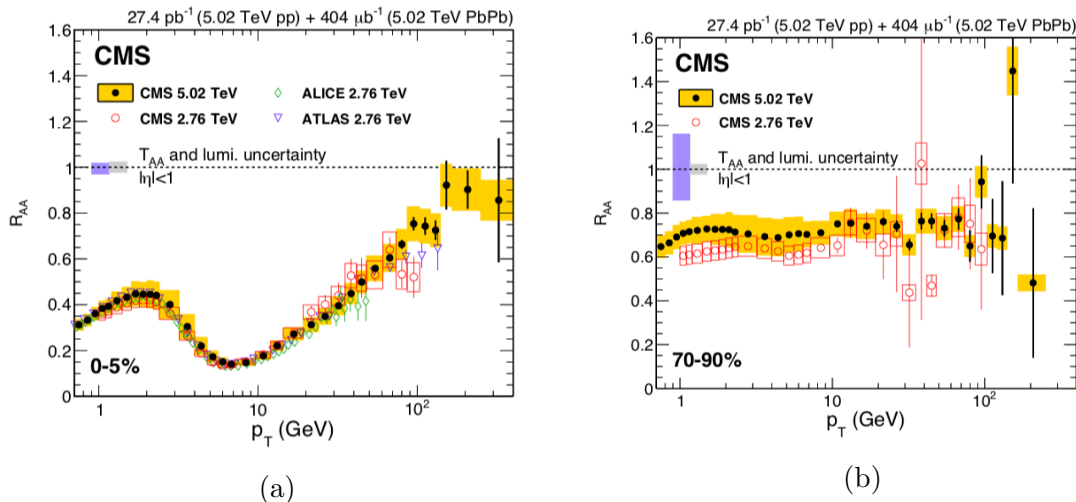


Figure 3.5: Nuclear modification factor, R_{AA} , for PbPb as a function of transverse momentum, p_T , for the two centrality classes (a) 0-5% and (b) 70-90%. The plots show results from two different collision energies, $\sqrt{s} = 2.76$ TeV and 5.02 TeV from CMS. Additional results from ALICE and ATLAS are shown for the most central case. The statistical uncertainties (error bars) and systematical uncertainties (boxes) are also shown. See text for further discussion about the plots. Figure from [22].

Figure 3.5 shows the nuclear modification factor for PbPb collisions as a function of transverse momentum, p_T . Figure 3.5a shows R_{AA} for the centrality class 0 – 5%, which is an average over the most central collisions. An observed suppression in the low- p_T regime can suggest a parton energy-loss due to medium interactions. Even though R_{AA} takes into account the number of collisions, it does not take medium interactions into consideration. Since this is a central collision, the number of participants is very high. Thus, a large droplet of medium can be created. Soft partons, i.e., particles with low momentum, loses energy due to medium interactions. Hard particles, however, have much more energy and is not as affected by the medium. Thus, as we can observe from the plot, R_{AA} is much closer to 1 for high- p_T . The

different collision energies considered ($\sqrt{s} = 2.76$ TeV and $\sqrt{s} = 5.02$ TeV) does not seem to affect the value of R_{AA} for the most central cases. Figure 3.5b shows the R_{AA} of very peripheral collisions in the centrality class 70 – 90%. Compared to the most central collisions, R_{AA} seems to be much closer to 1 in the low- p_T regime. Due to fewer participants in very peripheral collisions, the medium formed may not be as large as in the central collisions. Thus, the probability of interactions with the medium may be lower since there is a smaller area that can affect the parton energy. The values at larger p_T comes with very high uncertainties, but similar to the central case, these are also close to 1. The nuclear modification factor seems to be a little bit smaller for the collisions at lower energy, $\sqrt{s} = 2.76$ TeV, even when taken the systematical uncertainties into consideration. This might be because at lower collision energies, the low- p_T yields are larger. Since these are the one that gets most affected by medium interactions, the resulting R_{AA} is thus lower for lower collision energy compared to higher collision energy.

3.2.3 Jet-suppression

It can happen that two hard particles (particles with high momentum) collide with each other during the collision process, creating a back-to-back jet with high- p_T . Because of energy conservation, we would expect to observe two (almost) equally energetic jets on opposite sides in the detector. Figure 3.6 is an example of jet-suppression observed from the CMS detector. The figure shows transverse energy of final states as a function of rapidity and azimuthal angle. The jet is coloured red and is found by using a jet-finding algorithm. We observe one jet with high energy (leading jet), and one significantly smaller, suppressed jet (subleading jet). One may think of the plot as a cylinder wrapped around the ϕ -axis, where ϕ is the azimuthal angle of the beam axis (see Figure 3.7a for illustration). The pseudorapidity is defined as $\eta = -\ln[\tan(\theta/2)]$, where θ is the polar angle relative to the beam axis [23]. The collision take place at $\phi = \eta = 0$.

The polar angles to the jets in Figure 3.6 can be found by rewriting the expression for η , i.e., $\theta = 2\tan^{-1}[e^{-\eta}]$. For simplicity, we can approximate the values of η to be $\eta = -1$ (leading jet) and $\eta = 1$ (subleading jet), leading to the polar angles:

$$\theta_{\text{leading}} = 2\tan^{-1}[e^1] \frac{180}{\pi} \approx 140^\circ, \quad (3.2)$$

$$\theta_{\text{subleading}} = 2\tan^{-1}[e^{-1}] \frac{180}{\pi} \approx 40^\circ, \quad (3.3)$$

where $180/\pi$ is used to convert from radians to degrees. Both the azimuthal angle,

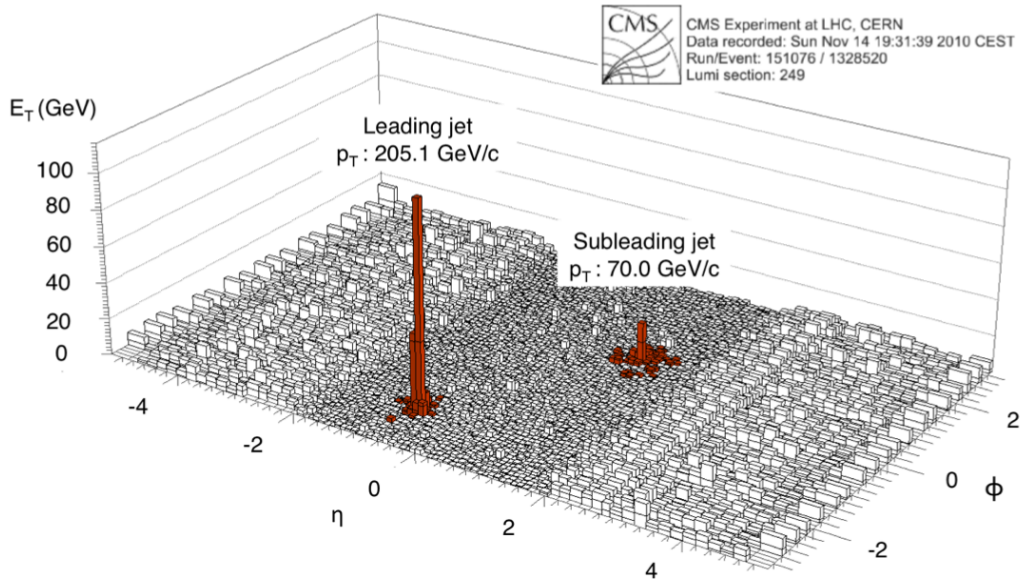
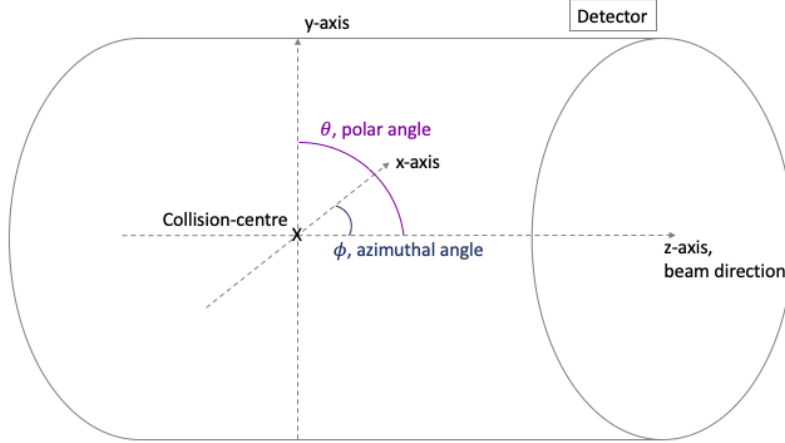


Figure 3.6: An example of observed jet-suppression. The transverse energy distribution in PbPb collision at $\sqrt{s} = 2.76$ TeV performed at the CMS detector at LHC, CERN. The collision happens at $\phi = \eta = 0$, where ϕ is the azimuthal angle and $\eta = -\ln[\tan\theta/2]$ is the pseudorapidity connected to the polar angle, θ . The observed jet-suppression of the back-to-back jet indicates medium creation in the collision. The subleading jet would have been affected by medium interactions, causing it to lose energy. Figure from [23].

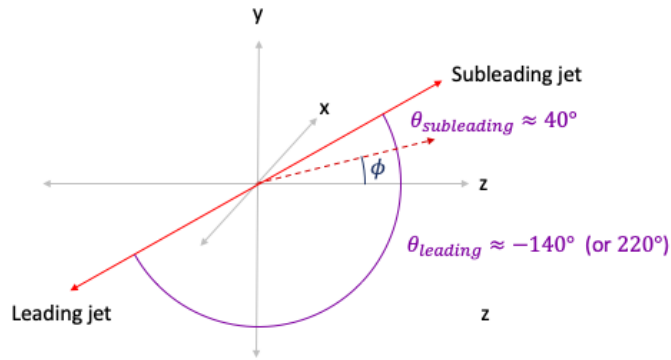
ϕ , and the pseudorapidity, η , for the leading jet are negative (seen in Figure 3.6), so the polar angle found must be negative. Thus, $\theta_{leading} \approx -140^\circ$ (or $\approx 220^\circ$). The angle between these two jets is therefore 180° , which we would expect due to energy-momentum conservation. Figure 3.7b is an illustration of how the two jets from Figure 3.6 look like in 3 dimensions.

Imagine pushing the η -axis from Figure 3.6 together and wrap it around the ϕ -axis (or, similarly, push the cylinder from Figure 3.7a together along the beam-axis). Then, we would get the energy distribution as a function of azimuthal angle, which is what Figure 3.4 displayed.

Jet-suppression may indicate the production of some medium during the evolution of the collision. The suppression of one of the jets can happen if the collision of the hard particles is oriented just the right way, say close to the surface of the medium. Then,



(a) The detector is shaped like a cylinder, when unwrapped gives the plot in Figure 3.6. The beam direction is shown together with the azimuthal angle as well as the polar angle, which is connected to the pseudorapidity in heavy-ion collisions.



(b) Illustration of the direction of the back-to-back jet from Figure 3.6 is given by the red arrow. I used the approximate values of $\eta = -1 \leftrightarrow \theta_{leading} \approx -140^\circ$ and $\eta = 1 \leftrightarrow \theta_{subleading} \approx 40^\circ$. The red, dotted line is the projection of the subleading jet onto the xz -plane and shows the azimuthal angle, ϕ . The difference in transverse energy is not taken into account.

Figure 3.7: Simplified illustration of the back-to-back jet created in the collision centre.

one of the jets will go straight out to the detector being highly energetic (leading jet), while the other will travel some distance through the medium before reaching the detector on the other side (subleading jet). The subleading jet will encounter energy-loss due to interactions with the medium before reaching the detector. In Chapter 4, we will look at a simple model for parton energy-loss due to medium interactions.

3.2.4 Strangeness enhancement

The last observable is the strangeness enhancement in AA-collisions compared to pp-collisions. Although I will not go into much details on this subject, I still think it is worth mentioning, so I will explain it shortly through the results provided in Figure 3.8.

Strangeness enhancement means a higher production of strange particles, which are particles build up by at least one strange quark, s . Figure 3.8 shows results from ALICE for pp-, pPb- and PbPb-collisions of yield ratios to pions as a function of final state particle density, $\langle dN_{ch}/d\eta \rangle$. On the left hand side we see the yield from pp-collision is increasing with particle density, and approaches the results from the small pPb-collisions. On the right hand side we observe the yields of PbPb-collisions with the collision energy, $\sqrt{s} = 2.76$ TeV. The yields are almost constant and is approaching the predicted values for thermal yields [25]. This may indicate that the strange particles produced in the heavy-ion collisions must originate from a thermal source, i.e. from QGP that gets created in these collisions. The fact that the yield from pp-collisions is lower supports this idea, as we know that no medium is formed in these small collisions.

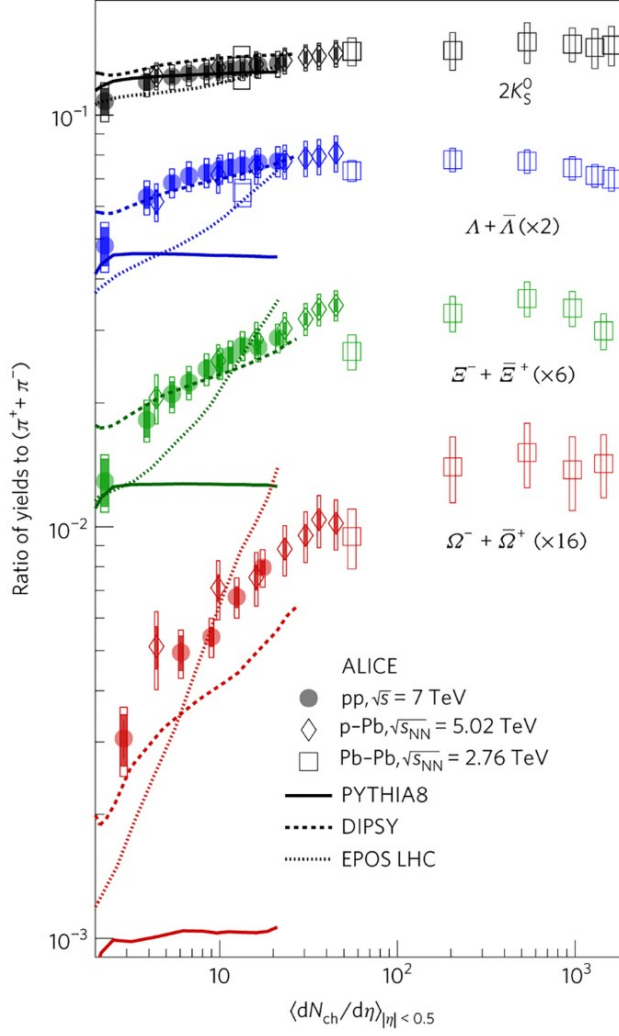


Figure 3.8: Strange particle production for pp-, pPb- and PbPb-collisions with statistical uncertainty (error bars) and total systematic uncertainty (empty boxes) are shown. Figure from [24].

Chapter 4

Energy-loss of a particle travelling through a medium

In this chapter, a parton energy-loss model by Arnold [1] is studied. This is a simple model, derived from the BDMPS-Z formalism, that provides the energy spectrum of emitted gluons of a hard particle due to soft interactions with a medium. The radiation of gluons is the same as how much energy the particle loses. The observables discussed in the previous chapter are based on final states of the collisions. This chapter considers two models of how the medium evolves and studies how the hard particle radiate energy (loses energy) leading to the final states observed.

4.1 Medium-induced gluon radiation

The basic picture is illustrated in Figure 4.1. A hard particle with energy, E , interacts with the medium which alters its transverse momentum with small changes, Δp_T . Over the total length travelled in the medium, L , the particle picks up a total change in its transverse momentum, called the transverse momentum broadening coefficient, $\hat{q} = \langle \Delta p_T^2 \rangle$. Each Δp_T comes from several small interactions along the medium. The medium is assumed to be finite, so after a length, L , the particle emerges into vacuum.

The general result for the medium-induced energy-loss spectrum is given by [1]

$$\omega \frac{d(I - I_{vac})}{d\omega} = \frac{\alpha}{\pi} x P_{s \rightarrow g}(x) \ln |c(0)|, \quad (4.1)$$

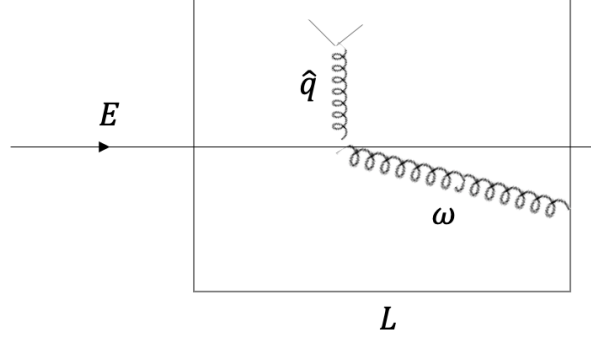


Figure 4.1: Incoming hard particle with energy E interact with the medium inside the brick with a total momentum \hat{q} and emits gluons with energy $\omega = xE$. We assume small x , which means a small fraction of the initial energy. The length of the medium/length travelled in the medium, L , is assumed to be finite.

where I is the probability of emission from the hard particle and I_{vac} is the probability that the emitted gluon is produced in vacuum. There is still much to be understood about I_{vac} . However, since this is a simple model, no further discussion about this is included. In the following, I will use the short-hand notation, I , representing the difference, $I - I_{vac}$.

The coupling constant is denoted by α and $\omega = xE$ is the energy of the emitted gluon. In the following, the assumption of small x is made. This means that we assume that the energy of the emitted gluon is very small compared to the initial energy of the particle. The splitting function, $P_{s \rightarrow g}$, is the probability of a particle of species s (quark or gluon) to split into a gluon.

For simplicity, the choice of gluon to gluon scattering inside the medium is used. Using a small x approximation, the splitting function can be written as

$$P_{g \rightarrow g}(x) = C_A \frac{1 + x^4 + (1 + x)^4}{x(1 - x)} \underset{\text{small } x}{\approx} \frac{2}{x} C_A, \quad (4.2)$$

where C_A is the Casimir of the adjoint representation and is used because we are considering $g \rightarrow g$ scattering. At the end of Section 1.1, C_A for the group $SU(3)$ was shown to have the value $C_A = N = 3$. Choosing a $q \rightarrow g$ scattering will only alter the splitting factor by some constant related to C_F , since quarks are described by the fundamental representation.

To avoid choosing a value for the coupling constant, α is factored out to the other side

of Eq.(4.1). In the small x approximation, Eq.(4.1) can then be expressed as

$$\frac{1}{\alpha}\omega\frac{dI}{d\omega} = \frac{2C_A}{\pi}\ln|c(0)|. \quad (4.3)$$

The function $c(t)$ must satisfy the differential equation

$$\frac{d^2c}{dt^2} = -\omega_0^2(t)c(t), \quad (4.4)$$

where $\omega_0(t)$ is a complex number. Eq. (4.4) has the following boundary conditions: $c(t) \rightarrow 1$ as $t \rightarrow \infty$ and $\dot{c}(t) = dc/dt = 0$ at $t \rightarrow \infty$. The complex number, $\omega_0(t)$, is related to the transverse momentum broadening coefficient, \hat{q} , by

$$\omega_0^2(t) = -i\frac{[(1-x)C_R + x^2C_R]\hat{q}(t)}{2x(1-x)E} \underset{\text{small } x}{\approx} -i\frac{C_R\hat{q}(t)}{2xE} = -i\frac{\hat{q}(t)}{2\omega}, \quad (4.5)$$

where we define $C_R\hat{q} = \hat{q}$ and C_R is the Casimir of the representation, R . The transverse momentum broadening coefficient, \hat{q} , is the average squared transverse momentum transfer, $\langle\Delta p_T^2\rangle$, the high energy particle picks up from medium interactions. Each transverse momentum picked up along the medium interactions follow Brownian motion. Thus, \hat{q} will increase with larger distance travelled in the medium. It can be worth noting the relation

$$|\omega_0(t)| = \sqrt{\frac{\hat{q}(t)}{2\omega}}, \quad (4.6)$$

following from Eq.(4.5), as it will be used in the following derivations.

Since the model used assume a finite medium, we must have that $\omega_0^2(t) \rightarrow 0$ as $t \rightarrow \infty$. This corresponds to the the particle leaving the medium and goes into vacuum at some point.

4.2 The "brick" (uniform, time-independent medium)

In this section, the simplest model of a medium is considered for simplicity. After we understand what happens in the case of a finite, uniform, time-independent medium, we can start studying more complicated medium profiles, as will be done in Section 4.4.

We start by looking at the radiation spectrum due to interactions inside a finite medium of length L which is uniform and time-independent. Such a medium is often referred to as a "brick" (see Figure 4.1). These conditions imply that the strength of the medium interaction is independent of time. Thus, $\hat{q}(t) = \hat{q}$ which also means that $\omega_0(t) = \omega_0$.

The particle will end up in vacuum after it has travelled through the medium of length L , so we have

$$\omega_0^2(t) = \begin{cases} \omega_0^2 = -i\frac{\hat{q}}{2\omega} & , t < L; \\ 0 & , t > L. \end{cases} \quad (4.7)$$

We want $c(t)$ to be continuous and smooth. By applying the boundary conditions: $c(L) = 1$ and $\dot{c}(L) = 0$, the analytical solution takes the form

$$c(t) = \begin{cases} \cos(\omega_0(L - t)) & , t < L; \\ 1 & , t > L. \end{cases} \quad (4.8)$$

The complex number, ω_0 , can be rewritten in terms of real values only by replacing $\sqrt{-i}$ in terms of a phase $e^{-i\pi/4}$. Thus, $\ln|c(0)|$ takes the form

$$\begin{aligned} \ln|c(0)| &= \ln|\cos(\omega_0 L)| \\ &= \ln|\cos(e^{-i\pi/4} |\omega_0| L)| \\ &= \frac{1}{2} \ln \left[\frac{1}{2} \cosh(\sqrt{2} |\omega_0| L) + \frac{1}{2} \cos(\sqrt{2} |\omega_0| L) \right], \end{aligned} \quad (4.9)$$

where we have used the identity from [1, Eq. 4.3] in the last step and $|\omega_0|$ is a real number defined by Eq.(4.6). Thus, the spectrum of the medium-induced radiation from a particle travelling through a brick is given by

$$\frac{1}{\alpha} \omega \frac{dI}{d\omega} = \frac{2C_A}{\pi} \frac{1}{2} \ln \left[\frac{1}{2} \cosh(\sqrt{2} |\omega_0| L) + \frac{1}{2} \cos(\sqrt{2} |\omega_0| L) \right]. \quad (4.10)$$

4.2.1 Asymptotic solutions

In this section, the asymptotic behaviour of Eq.(4.10) will be studied. First, the small and large L expansions of Eq.(4.9) is found. Then, these are compared to the asymptotic behaviour of the ω expansions. Since the spectrum is only a function of the ratio between the three parameter involved (\hat{q} , ω and L), we can write $|\omega_0|L = \frac{\hat{q}L^2}{2\omega} \propto \frac{L^2}{L_{cr}^2} \propto \frac{\omega_{cr}}{\omega}$, where L_{cr} and ω_{cr} are the critical values of the length and the emitted energy, which will be discussed more later. Thus, the critical values goes like $L_{cr} \propto \sqrt{\omega/\hat{q}}$ and $\omega_{cr} \propto \hat{q}L^2$.

Small L

For small L , or more precisely $|\omega_0|L \ll 1$, we first Taylor expand the terms inside the logarithm of Eq.(4.9), and then Taylor expand the remaining term. Thus, for a small medium/length travelled through the medium, we obtain

$$\begin{aligned}
\ln|c(0)| &\approx \frac{1}{2} \ln \left[\frac{1}{2} \left(1 + \frac{(\sqrt{2}|\omega_0|L)^2}{2!} + \frac{(\sqrt{2}|\omega_0|L)^4}{4!} + 1 - \frac{(\sqrt{2}|\omega_0|L)^2}{2!} + \frac{(\sqrt{2}|\omega_0|L)^4}{4!} \right) \right] \\
&= \frac{1}{2} \ln \left[1 + \frac{(\sqrt{2}|\omega_0|L)^4}{4!} \right] \\
&\approx \frac{(|\omega_0|L)^4}{12} = \frac{\hat{q}^2 L^4}{48\omega^2}.
\end{aligned} \tag{4.11}$$

Large L

Similarly, by looking at the large L behaviour ($|\omega_0|L \gg 1$), Eq.(4.9) goes like

$$\begin{aligned}
\ln|c(0)| &\approx \frac{1}{2} \ln \left[\frac{1}{2} \left(\frac{e^{\sqrt{2}|\omega_0|L}}{2} \right) + \frac{1}{2} \cos(\sqrt{2}|\omega_0|L) \right] \\
&\approx \frac{1}{2} \ln \left[\frac{1}{4} e^{\sqrt{2}|\omega_0|L} \right] \\
&= \frac{\sqrt{2}|\omega_0|L}{2} - \ln(2) \\
&\approx \frac{|\omega_0|L}{\sqrt{2}} = \sqrt{\frac{\hat{q}L^2}{4\omega}},
\end{aligned} \tag{4.12}$$

neglecting the $\ln(2)$ term since $|\omega_0|L \gg 1$.

Thus, the limiting cases for the medium-induced gluon radiation, Eq.(4.10), goes like

$$\frac{1}{\alpha} \omega \frac{dI}{d\omega} = \frac{2C_A}{\pi} \ln|c(0)| \approx \frac{2C_A}{\pi} \begin{cases} \frac{\hat{q}^2 L^4}{48\omega^2} & , \text{ for } |\omega_0|L \ll 1; \\ \sqrt{\frac{\hat{q}L^2}{4\omega}} & , \text{ for } |\omega_0|L \gg 1. \end{cases} \tag{4.13}$$

The critical value, L_{cr} , can be defined by the intersection point of the two asymptotic

solutions. Thus, by equating Eq.(4.11) and Eq.(4.12), we obtain

$$\begin{aligned} \frac{\hat{q}^2 L^4}{48\omega^2} &= \sqrt{\frac{\hat{q} L^2}{4\omega}} \\ \frac{\hat{q}^4 L^8}{48^2 \omega^4} &= \frac{\hat{q} L^2}{4\omega} \\ L^6 &= \frac{48^2 \omega^3}{4 \hat{q}} \\ L_{cr} &= 2 \sqrt[3]{3} \sqrt{\frac{\omega}{\hat{q}}}. \quad \left(\propto \frac{1}{|\omega_0|} \right) \end{aligned} \quad (4.14)$$

By assigning different values to $|\omega_0|$, the change of the radiation spectrum can be studied. In Figure 4.2, the spectrum for three different values of $|\omega_0|$ is shown. Since the spectrum only depends on the combination $|\omega_0|L$, the assigned values are in arbitrary units, for simplicity. The figure clearly show that by increasing $|\omega_0|$, L_{cr} decreases, which is consistent with what was shown in Eq.(4.14).

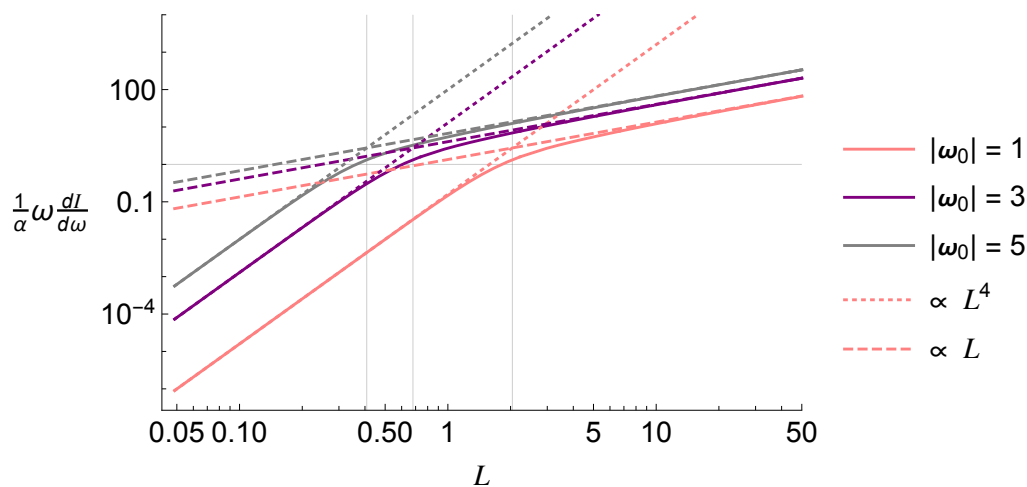


Figure 4.2: Radiation spectrum as a function of medium size/length travelled by the particle, L . The dotted (dashed) line corresponds to the small (large) L solutions found in Eq.(4.13). The critical value, L_{cr} , is shown as vertical lines crossing their intersection point. It will decrease with increasing value of the medium interaction strength, $|\omega_0|$, as shown in Eq.(4.14). The spectrum is dimensionless and since it only depends on the ratio $|\omega_0|L$, the units used is arbitrary, for simplicity.

Small ω

The small ω behaviour of the spectrum will now be discussed and connected to that of the medium size, L . Recall Eq.(4.6), where $|\omega_0| = \sqrt{\hat{q}/2\omega}$. Using this relation in the large L expansion, for which $|\omega_0|L \gg 1$, one can equally write

$$|\omega_0|L = \sqrt{\frac{\hat{q}L^2}{2\omega}} \gg 1 \quad \rightarrow \quad \frac{\hat{q}L^2}{2} \gg \omega. \quad (4.15)$$

Thus for large L , ω must be small. The asymptotic solution for large L therefore corresponds to the asymptotic solution for small ω . The spectrum in the low- ω regime can therefore be expressed as

$$\frac{1}{\alpha}\omega \frac{dI}{d\omega} \approx \frac{2C_A}{\pi} \sqrt{\frac{\hat{q}L^2}{4\omega}} \quad , \text{ for } \omega \ll 1. \quad (4.16)$$

Large ω

Following the same steps as above, the large ω expansion for the spectrum is found. Since one can write $|\omega_0|L = \sqrt{\hat{q}L^2/2\omega} \ll 1$ (for the large L expansion), one finds $\hat{q}L^2/2 \ll \omega$. Thus, when L is small, ω must be large. Consequently, the large ω expansion for the spectrum goes like the small L expansion. Namely, in the large ω regime, the spectrum goes like

$$\frac{1}{\alpha}\omega \frac{dI}{d\omega} \approx \frac{2C_A}{\pi} \frac{\hat{q}^2 L^4}{48\omega^2} \quad , \text{ for } \omega \gg 1. \quad (4.17)$$

The critical value, ω_{cr} , can be defined in the same fashion as L_{cr} . Equating Eq.(4.16) and Eq.(4.17), we obtain

$$\begin{aligned} \sqrt{\frac{\hat{q}L^2}{4\omega}} &= \frac{\hat{q}^2 L^4}{48\omega^2} \\ \frac{\hat{q}L^2}{4\omega} &= \frac{\hat{q}^4 L^8}{48^2 \omega^4} \\ \omega^3 &= \frac{4}{48^2} \hat{q}^3 L^6 \\ \omega_{cr} &= \frac{\hat{q}L^2}{4 \times 3^{2/3}}. \end{aligned} \quad (4.18)$$

Combining Eq.(4.16) and Eq.(4.17) into one and rewriting in terms of the critical energy, ω_{cr} , the spectrum for induced gluon emission takes the form

$$\frac{1}{\alpha} \omega \frac{dI}{d\omega} \approx \frac{2C_A}{\pi} \begin{cases} \sqrt{\frac{\hat{q}L^2}{4\omega}} \propto \sqrt{\frac{\omega_{cr}}{\omega}} & , \omega \ll \omega_{cr} ; \\ \frac{\hat{q}^2 L^4}{48\omega^2} \propto \left(\frac{\omega_{cr}}{\omega}\right)^2 & , \omega_{cr} \ll \omega . \end{cases} \quad (4.19)$$

Figure 4.3 shows the spectrum as a function of emitted energy, ω , for different values of L , i.e., for different lengths travelled through the medium. For simplicity, the units used are arbitrary. In this figure, I want to show how ω_{cr} in fact does increase with medium size, as expected from Eq.(4.18). Thus, for longer time in the medium, the probability of emitting a gluon of higher energy also increases.

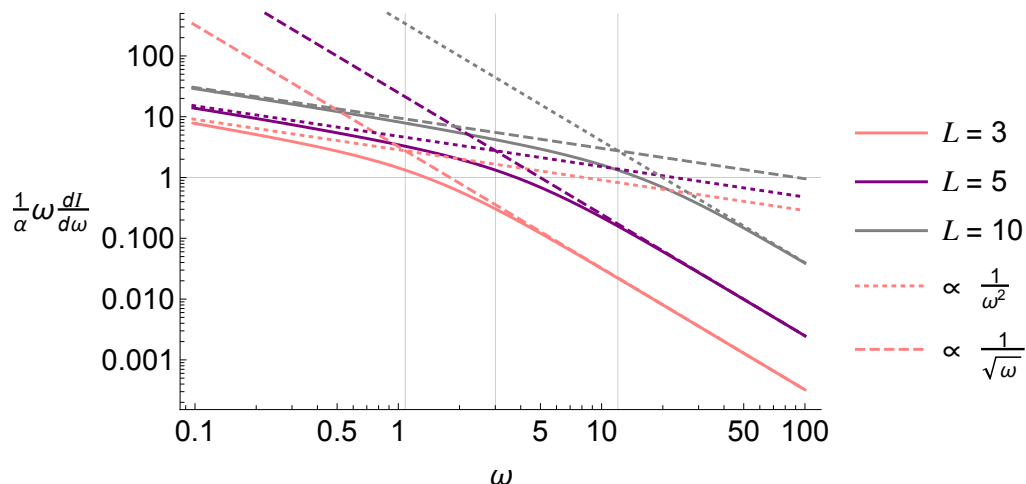


Figure 4.3: Medium-induced gluon radiation spectrum, Eq.(4.1), as a function of emitted energy, ω . Asymptotic solutions for small (large) ω are shown as dotted (dashed) lines. The gray vertical lines corresponds to the critical value, ω_{cr} , found at their intersection point. In agreement with Eq.(4.18), ω_{cr} increases with increasing medium size/length travelled inside the medium. Since $dI/d\omega$ is the probability of emitting a gluon of energy ω , $\omega dI/d\omega$ is a measure of how many gluons are emitted at that energy. Note that at ω_{cr} , the spectrum is approximately 1. This will be discussed further in the next section.

4.3 From medium-induced radiation spectrum to the energy-loss of a particle

The spectrum of emitted gluons, Eq.(4.1), is a measure of how much radiation comes from different emitted energies, ω . By integrating over all ω , we obtain the total energy-loss of the hard particle. The only combination of the variables at hand is $\frac{\hat{q}L^2}{\omega}$. A quick dimensional analysis shows that: $\frac{(\text{GeV})^2 \text{ fm}^2}{\text{fm GeV}} = \text{GeV fm} \approx 5$ ¹. This tells that the energy-loss only depends on the dimensionless ratio of the three parameters involved. Using Eq.(4.19), we find that the energy-loss scales like:

$$E = \int d\omega \omega \frac{dI}{d\omega} \approx \frac{2\alpha C_A}{\pi} \left[\sqrt{\frac{\hat{q}L^2}{4}} \int_0^{\omega_{cr}} d\omega \frac{1}{\sqrt{\omega}} + \frac{\hat{q}^2 L^4}{48} \int_{\omega_{cr}}^{\infty} d\omega \frac{1}{\omega^2} \right] \quad (4.20)$$

$$= \frac{2\alpha C_A}{\pi} \left[\sqrt{\frac{\hat{q}L^2}{4}} 2\sqrt{\omega_{cr}} + \frac{\hat{q}^2 L^4}{48} \frac{1}{\omega_{cr}} \right] = \frac{2\alpha C_A}{\pi} \left[2\sqrt[3]{3}\sqrt{\omega_{cr}}\sqrt{\omega_{cr}} + \sqrt[3]{3}\omega_{cr}^2 \frac{1}{\omega_{cr}} \right] \quad (4.21)$$

$$= \frac{6\sqrt[3]{3}\alpha C_A}{\pi} \omega_{cr}. \quad (4.22)$$

In Eq.(4.20), an estimate of the total energy-loss was done by inserting the two asymptotic solutions, found in the previous section, since the integrals will be dominated by the upper and lower limits. The definition of the critical emission energy, $\omega_{cr} = \frac{\hat{q}L^2}{4 \times 3^{2/3}}$, was applied in Eq.(4.21). From Eq.(4.22), one can see that the energy-loss scales like ω_{cr} , meaning that the average energy of the emitted gluon will have its value around ω_{cr} . As shown in Fig. 4.3, ω_{cr} will increase with medium size. Thus, the energy-loss of a particle will increase with increasing distance travelled through a medium.

Probability of radiation and number of emitted gluons

The probability of emitting a gluon of energy ω is given by $dI/d\omega$. Thus, multiplying the probability by ω provides the number of produced particles of this energy. One

¹In natural units, $c = \hbar = 1$, so the conversion constant $\hbar c = 197.3 \text{ MeV fm}$, taken from CODATA [26], gives $1\text{fm} = \frac{1}{0.1973} \text{GeV}^{-1} = 5.0684 \text{GeV}^{-1}$. Thus, $\text{GeV fm} = 5.0684 \approx 5$.

can observe from Fig. 4.3, that most of the emitted gluons have very low energies ($\omega \ll \omega_{cr}$) and the particle will emit very few high-energy gluons ($\omega \gg \omega_{cr}$). If one takes the average, there will be emitted one particle of energy ω_{cr} , and is why the total energy-loss scales like this value.

If the hard particle splits into two, i.e., if only one gluon is emitted in the process, the energy of the emitted gluon, ω_{split} , can be found using $\omega \, dI/d\omega \propto \sqrt{\omega_{cr}/\omega_{split}} = 1$, because we only consider the hard particle to emit one gluon. Rewrite in terms of the splitting energy one gets, $\omega_{split} = \omega_{cr} \propto \hat{q}L^2$. Thus, the energy-loss of the hard particle in this process will be $E \propto \hat{q}L^2$. The length the hard particle has to travel before emitting a gluon of this energy is found by rewriting the previous expression: $L \propto \sqrt{\frac{E}{\hat{q}}}$.

Example

Imagine that the hard particle travels through an infinitely long medium. We will now try to understand what will happen to that particle. The formation time, t_{form} , is the time it takes a gluon emission to "separate" from a particle (see Figure 4.4a for illustration). During the splitting time, t_{split} , the hard particle can be affected by several soft gluon emissions with a probability, α , due to medium interactions. The total splitting times is then connected to the formation time by $t_{split} = \alpha t_{form}$.

In the previous section, the connection, $E \propto \hat{q}L^2$, between the energy-loss and the length travelled in the medium was made. This can also be expressed in terms of the splitting time, $t_{split} = L \propto \sqrt{\frac{E}{\hat{q}}}$. Thus, the time it takes to split a particle with energy E to half its energy is $t_{split} \propto \sqrt{E/\hat{q}}$. The time it takes to split the particle with energy $E/2$ in half will then be $t_{split} \propto \sqrt{E/2\hat{q}}$, and so on (see Figure 4.5 of the simplified idea).

If one considers the medium to be infinitely long, the particle can continue to split like this using the time

$$t = t_{split} \left(1 + \frac{1}{\sqrt{2}} + \frac{1}{\sqrt{4}} + \frac{1}{\sqrt{8}} + \dots \right), \quad (4.23)$$

which is a geometric series that can be expressed as (using $x = \sqrt{2}$):

$$\sum_{n=0}^{\infty} \frac{1}{\sqrt{2}^n} = \frac{\sqrt{2}}{\sqrt{2}-1} = 2 + \sqrt{2}. \quad (4.24)$$

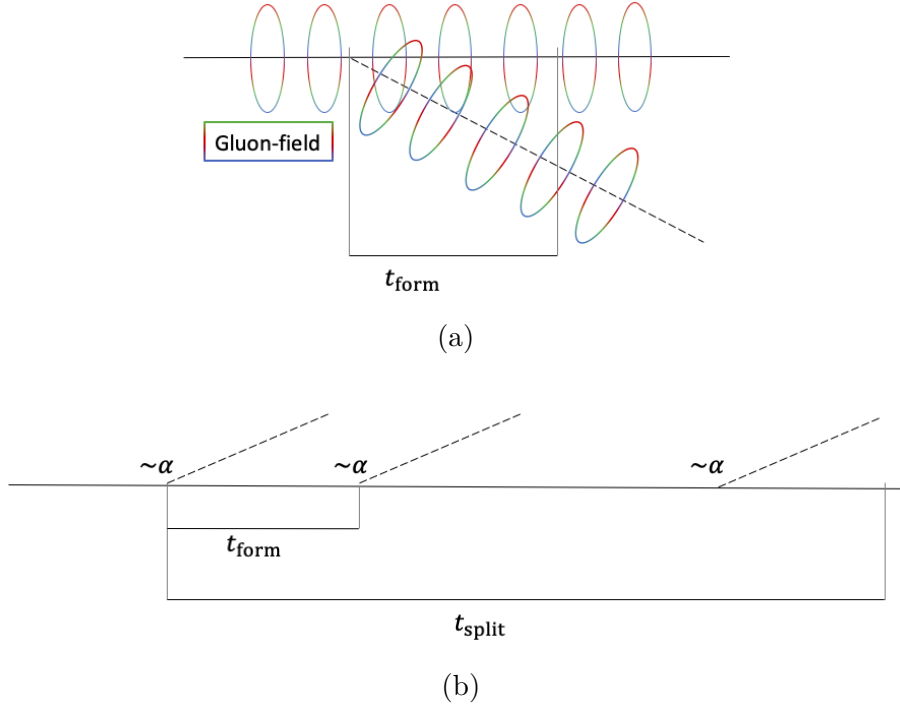


Figure 4.4: Illustration of the formation time, t_{form} , and how this is related to the splitting time, t_{split} , between each scattering that comes with probability of α . (a) The formation time is the time it takes the two particles to be separated into distinct particles, i.e., when their gluon fields do not overlap anymore. (b) Each radiation comes with a factor of α . The splitting time is related to the formation time by $t_{\text{form}} = \frac{1}{\alpha} t_{\text{split}}$.

After a time $t = t_{\text{split}}(2 + \sqrt{2})$, the hard particle have been divided in half so many times that it is now indistinguishable from the medium and we cannot see any radiation from the emitted gluons. If the splitting of the particle is oriented such that one of the particles is directed straight out of the medium, and its counterpart travels a long time through the medium, this can be an explanation to why we do not observe radiation on the other side. If they are not directed as such, we may observe similar strengths of the radiation on both sides.

In this example, the consideration of an infinitely long medium was done. If one instead look at a finite medium, which is more realistic, the hard particle may not have the time to "disappear" completely. However, one of the emitted rays may loose a significantly amount of energy due to medium interactions, and can be one

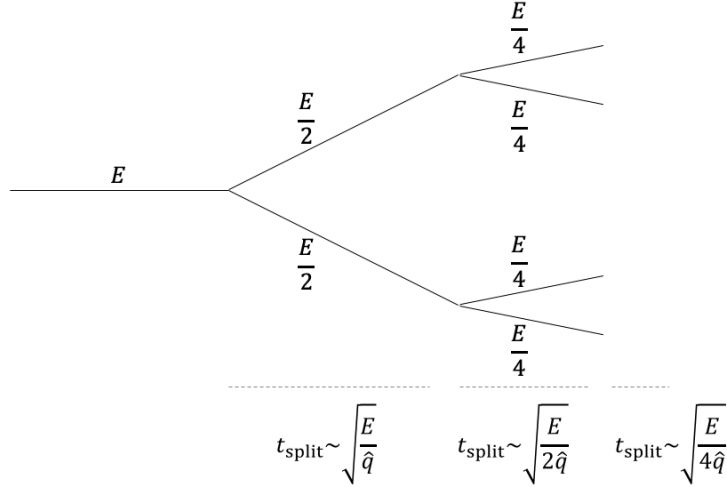


Figure 4.5: Splitting of a hard particle with energy E into two during a splitting time, t_{split} .

explanation of the observed jet-suppression from Fig. 3.6, discussed in the previous chapter.

4.4 Power-law (time-dependent medium)

Since the medium formed in heavy-ion collisions is a fast expanding quark-gluon plasma, ideally we want to have a model of the medium evolution as similar to that as possible. However, such a model can be very complex, containing spots of different energy-density as well as it is expanding in time. A good way to start understanding how particles loses energy in QGP, is by considering a uniform, time-dependent medium. From this point of view, it may be easier to understand a more complicated profile, which is left for future study.

In this section, a uniform, time-dependent medium will be considered. This implies that $\hat{q} = \hat{q}(t)$ and $w_0^2 = w_0^2(t)$. The medium-induced effects will drop with some power, a , of time. The transverse broadening coefficient is $\hat{q}(t) = \hat{q}_0 (t_0/t)^a$, where \hat{q}_0 is the initial value of the medium interaction. The particle emerges into vacuum after length L . The medium-induced radiation will be found for different values of a and compared to the asymptotic solutions, which in this section if found using a general formula from [1]. At the end of this section, a comparison is also drawn to the time-independent medium, the brick.

We have:

$$\omega_0^2(t) = \begin{cases} -i \frac{\hat{q}(t)}{2\omega} = -i \frac{\hat{q}_0}{2\omega} \left(\frac{t_0}{t}\right)^a & , t_0 < t < t_0 + L; \\ 0 & , t_0 + L < t; \end{cases} \quad (4.25)$$

where t_0 is the initial time of the emitted particle (for the brick we used that $t_0 = 0$) and \hat{q}_0 is a real number. Using the same boundary conditions as before, $c(t) = 1$ and $\dot{c}(t) = 0$ for $t > t_0 + L$, i.e. the particle emerges into vacuum after $t_0 + L$ in the medium, we borrow the solution to the differential equation, Eq.(4.4), from Arnold [1, Eq.4.12]:

$$c(t) = \begin{cases} \left(\frac{\pi z_L}{2}\right)^\nu \left(\frac{z}{z_L}\right)^\nu [J_\nu(z)Y_{\nu-1}(z_L) - Y_\nu(z)J_{\nu-1}(z_L)] & , t_0 < t < t_0 + L; \\ 1 & , t_0 + L < t, \end{cases} \quad (4.26)$$

where

$$\begin{aligned} \nu &\equiv \frac{1}{2-a}, \\ z = z(t) &\equiv 2\nu\omega_0 t_0 \left(\frac{t}{t_0}\right)^{1/2\nu}, \\ z_0 &\equiv z(t_0), \\ z_L &\equiv z(t_0 + L). \end{aligned}$$

Asymptotic solutions

General solutions for the limiting cases for small and large L behaviour is taken from [1]. The reference uses the value $t_0 = 0$. However, since I am using a power-law, which goes like $\sim 1/t$, I have rewritten the equations in terms of a general initial time, t_0 . Then, Eq.(4.27) and Eq.(4.29) are two general solutions for the medium-induced spectrum. The following derivation is made for the value $a = 1$.

Small L

Implementing Eq.(4.6) in the general solution for small lengths travelled through the medium, the spectrum of the emitted particle will go like

$$\begin{aligned}
\ln|c(t_0)| &\simeq \frac{1}{2} \left[\int_{t_0}^{\infty} dt(t-t_0)|\omega_0^2(t)| \right]^2 \\
&\quad - \int_{t_0}^{\infty} dt(t-t_0)|\omega_0^2(t)| \int_t^{\infty} dt'(t'-t)|\omega_0^2(t')| \\
&= \frac{1}{2} \left[\int_{t_0}^{t_0+L} dt(t-t_0) \frac{\hat{q}_0 t_0}{2\omega t} \right]^2 \\
&\quad - \int_{t_0}^{t_0+L} dt(t-t_0) \frac{\hat{q}_0 t_0}{2\omega t} \int_t^{t_0+L} dt'(t'-t) \frac{\hat{q}_0 t_0}{2\omega t'} \\
&= \frac{1}{2} \left(\frac{\hat{q}_0 t_0}{2\omega} \right)^2 \left[\int_{t_0}^{t_0+L} dt \left(1 - \frac{t_0}{t} \right) \right]^2 \\
&\quad - \left(\frac{\hat{q}_0 t_0}{2\omega} \right)^2 \int_{t_0}^{t_0+L} dt \left(1 - \frac{t_0}{t} \right) \int_t^{t_0+L} dt' \left(1 - \frac{t}{t'} \right) \\
&= \left(\frac{\hat{q}_0 t_0}{2\omega} \right)^2 \frac{1}{4} \left[L(L-6t_0) + 2t_0^2 \left(-3\ln(t_0) + \ln\left(\frac{t_0}{t_0+L}\right)^2 + 3\ln(L+t_0) \right) \right] \\
&\sim \frac{\hat{q}_0^2 L^4}{\omega^2}, \tag{4.28}
\end{aligned}$$

where the upper limit $t_0 + L$ has been used since $|\omega_0| = 0$ for $t > t_0 + L$.

Large L

Next, we look at the large L behaviour of Eq.(4.6). The medium-induced spectrum goes like

$$\begin{aligned}
\ln|c(t_0)| &\simeq \frac{1}{\sqrt{2}} \int_{t_0}^{\infty} dt |\omega_0(t)| & (4.29) \\
&= \frac{1}{\sqrt{2}} \int_{t_0}^{t_0+L} dt \sqrt{\frac{\hat{q}_0 t_0}{2\omega t}} \\
&= \sqrt{\frac{\hat{q}_0 t_0}{4\omega}} \left[2(\sqrt{t_0 + L} - \sqrt{t_0}) \right] \\
&\sim \sqrt{\frac{\hat{q}_0 L^2}{\omega}}. & (4.30)
\end{aligned}$$

Thus, the medium-induced radiation spectrum at small and large L (or similarly $|\omega_0|L$) will go like

$$\frac{1}{\alpha} \omega \frac{dI}{d\omega} \propto \begin{cases} \frac{\hat{q}^2 L^4}{\omega^2} & , |\omega_0|L \ll 1; \\ \sqrt{\frac{\hat{q} L^2}{\omega}} & , |\omega_0|L \gg 1. \end{cases} \quad (4.31)$$

Small and large ω behaviour of the spectrum

In the same fashion as the small and large ω behaviour of the spectrum for the brick-profile where deduced (on page 46), the same can be done in this case. Using the relation $|\omega_0| = \sqrt{\hat{q}/(2\omega)}$, the asymptotic behaviour for the spectrum can be found. For a small system, for which $|\omega_0|L \propto \sqrt{\hat{q}L^2/\omega} \ll 1$, one can rewrite and find $\hat{q}L^2 \ll \omega$. Thus, for small L , ω must be large. This means that the small L behaviour is the same as the large ω behaviour of the spectrum.

The same can be shown for the other limiting case, namely that the large L behaviour is the same as the small ω behaviour. I will rewrite the asymptotic solutions using ω_{cr} since this is proportional to $\hat{q}L^2$. Thus, the medium-induced spectrum as function of emitted energy, ω , will go like

$$\frac{1}{\alpha} \omega \frac{dI}{d\omega} \propto \begin{cases} \sqrt{\frac{\omega_{cr}}{\omega}} & , \omega \ll \omega_{cr}; \\ \left(\frac{\omega}{\omega_{cr}}\right)^2 & , \omega \gg \omega_{cr}. \end{cases} \quad (4.32)$$

I have solved the medium-induced radiation for some given values of t_0 , L and \hat{q} (in arbitrary units). The results are shown in Figure 4.6. The spectrum fits very

well with the limiting solutions found in Eq.(4.32). In the intersection-point of the small and large ω , is the point $\omega_{critical}$. This is the average energy of the emitted particles. As the value of a increases, ω_{cr} decreases. This is because the medium effects drops faster, recall that $\hat{q}_0(t) \propto 1/t^a$, so we can think of the particle travelling a shorter distance in the medium. Thus, increasing a will be as if the medium size, L , decreased. This can also be seen by comparing Figure 4.6 and Figure 4.2.

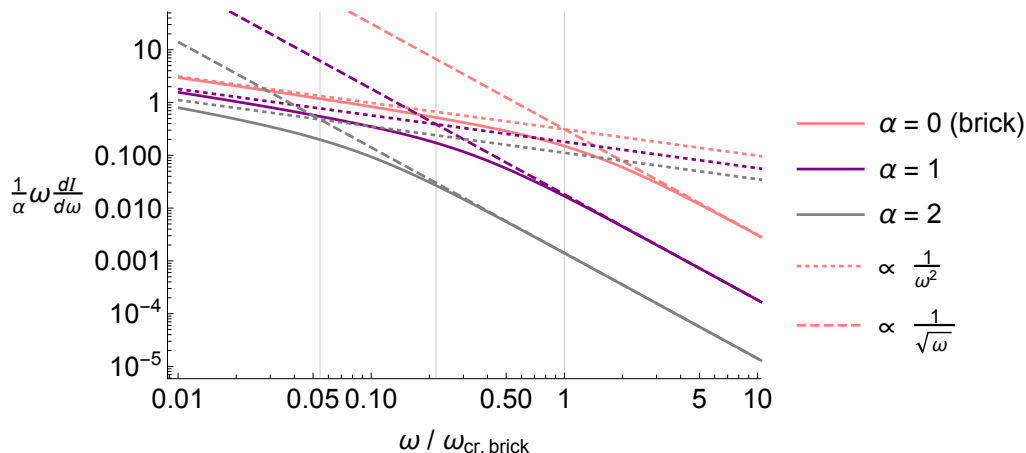


Figure 4.6: Spectrum from medium-induced radiation, $\omega dI/d\omega$ (divided by α), as a function of emitted energy for different values of a . The x -axis is $\omega/\omega_{cr,brick}$, where $\omega_{cr,brick}$ is the critical value derived for the brick (i.e. for the case where $a = 0$). The dotted lines corresponds to the asymptotic behaviour for small ω behaviour of the spectrum and goes like $1/\omega^2$, as found in Eq.(4.30). The asymptotic behaviour for large ω goes like $1/\sqrt{\omega}$, as found in Eq.(4.28), and are shown as dashed lines. The gray, vertical lines are the corresponding critical energies for the different values of a . This value decreases for increasing value of a , because the medium effects drops faster, making the medium seem smaller/shorter. This can also be seen by comparing this figure to the similar behaviour of the critical points observed in Fig. 4.2.

Another thing that is interesting when looking closely at the very small ω regime of Fig. 4.6, is how the asymptotic solution starts to deviate more and more from the spectrum as the value of a increases. Recall that small ω behaviour was the same as the large L behaviour of the spectrum. Thus, by increasing the value of a , the spectrum starts to deviate from the large L solution. In the next section, this trend will be looked at when the determination of a critical value of a is found.

4.5 Comparing different mediums: Brick vs. Power-law

In this section, the spectrum for the power-law will be compared to that of the brick. I will also determine the approximate value of a for which the asymptotic solution for small ω deviates from the spectrum.

The brick was defined through the time-independent transverse momentum broadening coefficient, \hat{q}_{eff} . One can also get to the brick through the power-law by choosing $a = 0$, then, $\hat{q}(t) = \hat{q}_0(t_0/t)^{a=0} = \hat{q}_{\text{eff}}$.

If one were to apply the general solutions, Eq.(4.27) and Eq.(4.29), to the brick-profile, one obtain the same results which where found using small and large expansions. This will be done on page 60 and 62. Thus, the general solutions provided by [1], seem to work very well, at least in the case for small values of a .

In the following, I will try to find the critical value of a for which the asymptotic behaviour of the small ω -regime deviates from the spectrum. This trend was seen for increasing values of a at very small ω in Fig. 4.6 and can be seen to a greater extent in Figure 4.7.

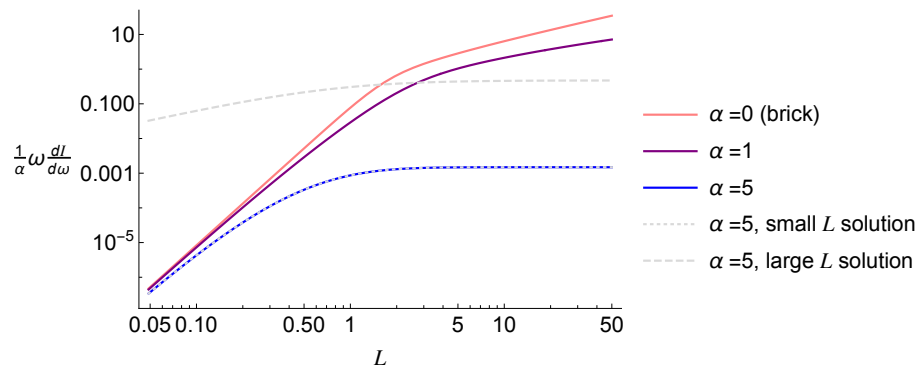


Figure 4.7: Medium-induced radiation spectrum as a function of L for different values of a . The limiting solutions for $a = 5$ is found using Eqs.(4.27) and (4.29) and are showed as dotted/dashed lines. Recall that looking at the large L behaviour is the same as studying the small ω -behaviour. For $a = 1$, the spectrum looks very similar to that of the brick ($a = 0$). For $a = 5$, the function goes like the limiting solution for small L . This is because the medium effects drops so quickly, that one can think of the particle going through a shorter medium. Thus, it makes sense that the spectrum for large a goes like a small medium.

This is because $\hat{q}(t)$ drops very rapidly, meaning that the interaction from the medium will rapidly decrease and thus barely affect the particle after a short time (length). After a short time, it will be like the medium is not there at all, so it makes sense that it looks like the small L approximation. Increasing the length will not give a larger energy-loss. This can also be seen in Figure 4.8, where $\ln|c(t_0)|$ goes to a constant when $L \rightarrow \infty$.

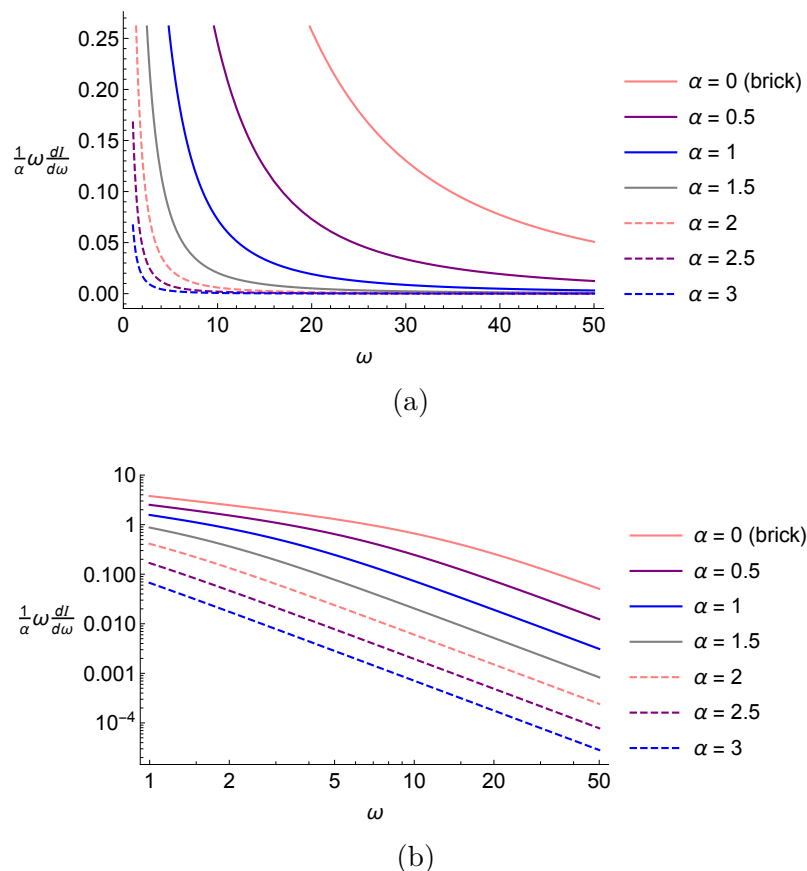


Figure 4.8: (a) Medium-induced radiation spectrum as a function of ω for different values of a . (b) LogLogPlot of (a). The straight lines in the LogLogPlot means that the function is not changing. E.g. for the $a = 0$ (brick), the spectrum changes from the asymptotic solutions $\sim 1/\sqrt{\omega}$ to $\sim 1/\omega^2$ which is shown in the LogLogPlot as the bend of the spectra (around ω_{cr}). The fact that for $a \geq 2$, the plots are very close to linear, means that these are the values for which the asymptotic solution deviate from the spectrum.

By dimensional analysis, the value of a for which the small L approximation equals the large L approximation is found. Using Eq.(4.27) and Eq.(4.29), the two asymptotic solutions goes like:

$$\ln|c(t_0)| \stackrel{L \ll 1}{\sim} \left[\int_{t_0}^{t_0+L} dt (t - t_0) |\omega_0^2| \frac{t_0^a}{t^a} \right]^2 \sim \left[L(L - 1) \frac{1}{L^a} \right]^2 \sim L^{4-2a}, \quad (4.33)$$

and

$$\ln|c(t_0)| \stackrel{L \gg 1}{\sim} \int_{t_0}^{t_0+L} dt |\omega_0| \sqrt{\frac{t_0^a}{t^a}} \sim L \frac{1}{L^{a/2}} \sim L^{1-a/2}. \quad (4.34)$$

Equating the powers, we get that

$$4 - 2a = 1 - a/2 \rightarrow a = 2. \quad (4.35)$$

Thus, for $a \geq 2$, the medium-induced effects will drop fast enough that increasing the length travelled through the medium will not contribute much to the spectrum. Figure 4.8a shows the spectra as a function of emitted energy, ω , for different values of a . We see that close to the value $a = 2$, the spectrum is rapidly decreasing. Figure 4.8b is a loglogplot of the same functions. It is easier to see where the spectrum is going from a curved line to an (almost) straight line, indicating that the function itself goes to a constant.

4.6 Scaling laws

In this section, different scaling laws will be studied. The scaling law provided by Salgado and Wiedemann [2] is one way of finding the spectrum for a time-dependent medium using the simple analytical solution for the brick, Eq.(4.8). The accuracy of this scaling law will now be checked against the solution for a time-dependent medium given by Arnold [1], Eq.(4.26). In addition, I will derive two new scaling laws, look at their accuracy and compare them to the formula provided by [2].

The idea behind the scaling law is as follows: One can find the radiation spectrum to a particle travelling through a time-dependent medium following a power-law, by defining an initial value \hat{q}_0 and a . The analytical solution to the function $c(t_0)$ is given by Eq.(4.26), which is used in the final equation determining the spectrum. The scaling law is an equation relating the \hat{q}_0 and a used in the complicated solution, to the effective broadening \hat{q}_{eff} used in the much simpler analytical solution given by Eq.(4.8): $c(0) = \cos(\sqrt{\hat{q}_{\text{eff}}/2\omega}L)$. This means that a radiation spectrum in the brick

(using a \hat{q}_{eff}) can equivalently be found using the power-law solution by [1], Eq.(4.26) (using \hat{q}_0). The spectrum using the scaling laws are compared to the solution found by [1], and compared for the three different values of a . The accuracy of the different scaling laws varies along different regimes of the radiation spectrum.

4.6.1 Salgado and Wiedemann

The scaling law provided by Salgado and Wiedemann [2] is rewritten to match the notation used in this paper. It is given by

$$\hat{q}_{\text{eff}} = \frac{2\hat{q}_0}{L^2} \int_{t_0}^{t_0+L} dt (t - t_0) \left(\frac{t_0}{t}\right)^a. \quad (4.36)$$

Salgado and Wiedemann did not have the analytical solution to the power-law, which we borrowed from [1] in Eq.(4.26). So the idea is that the spectrum one would get by considering a medium which drops like the power-law for a given a and some value of \hat{q}_0 , would give the same spectrum as if one used the analytical solution for the brick, Eq.(4.8) with a \hat{q}_{eff} determined by the scaling law, Eq.(4.36). When computing the different spectra, I assigned a value to the effective \hat{q}_{eff} to the brick solution. Then, \hat{q}_0 was determined for different values of a by Eq.(4.36). This was done so that all spectra would match the same scaled brick-spectrum. Whether one finds \hat{q}_{eff} for the brick by defining \hat{q}_0 or define \hat{q}_{eff} and then find the corresponding \hat{q}_0 for different a will give the same results. When finding the different spectra from this scaling law, I used the value $\hat{q}_{\text{eff}} = 3.2$ in arbitrary units for the brick spectrum. The resulting \hat{q}_0 and the corresponding spectra for different values of a are shown in Figure 4.9.

The x -axis of Fig. 4.9 is in $\omega/\omega_{cr,\text{brick}}$, where $\omega_{cr,\text{brick}}$ is the critical value derived for the brick. The accuracy of the scaling law provided by Salgado and Wiedemann seems to be overall very good. The spectra for the scaled brick are very close to the ones found for different values of a . For very small ω and $\omega > \omega_{cr}$, the scaled spectrum shows more deviations, so there is still room for improvements.

4.6.2 Small ω scaling

In this section, I will derive a new scaling law by using the small ω expansion of the medium-induced spectrum, Eq.(4.29). Since the ratio of the spectra will be used, the factor of $2\alpha C_A/\pi$ will cancel. Thus, one only need to find the expansions for $\ln|c(t_0)|$.

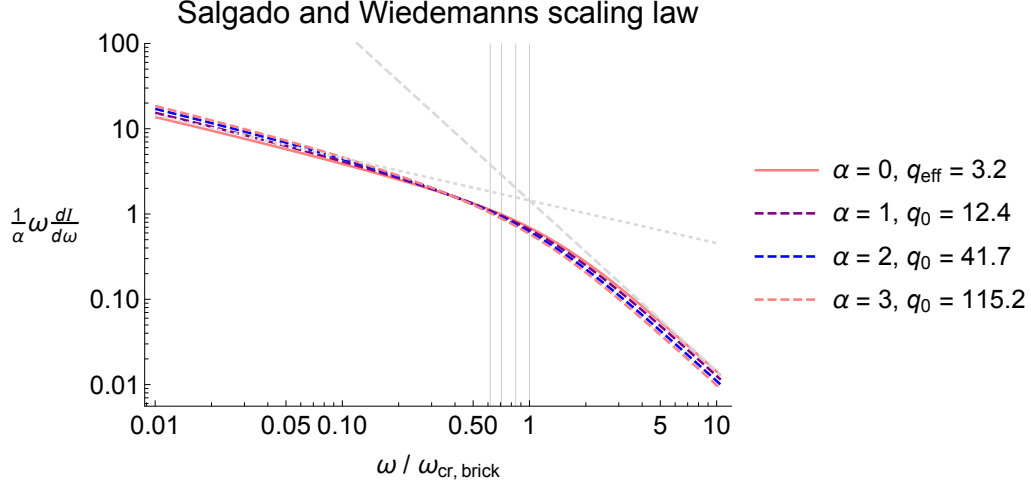


Figure 4.9: This figure shows how accurate the scaling law by Salgado and Wiedemann is. The dotted lines are found using the solution to the power-law, given by [1], with the given values of \hat{q}_0 and a . The pink line ($a = 0$) is the corresponding spectrum using \hat{q}_{eff} defined by Eq.(4.36). To have all the spectra compare to the same brick-spectra, I used Eq.(4.36) "the other way around". Starting with a given value for the effective broadening, $\hat{q}_{\text{eff}} = 3.2$ in arbitrary units, and then found the corresponding \hat{q}_0 (if I had used the same \hat{q}_0 for the different a , I would have gotten three different brick-solutions). The asymptotic solutions are shown for $a = 0$ (brick) and the intersection point of these, which occurs at 1, is our definition of $\omega_{cr,brick}$. The x -axis is scaled by $\omega/\omega_{cr,brick}$. The gray vertical lines corresponds to $\omega_{cr}/\omega_{cr,brick}$ for each value of a . It decrease with increasing a . By noticing how close these values are to 1, one can see that this scaling gives a good approximation. However, as the critical values is shifted from 1, so is the spectra, making it a little bit worse at the two ends of the figure.

Solving the integral, the small ω expansion for the brick takes the form:

$$\begin{aligned}
\ln|c(t_0)|^{(\text{brick})} &= \frac{1}{\sqrt{2}} \int_{t_0}^{t_0+L} dt |\omega_0(t)| \\
&= \frac{1}{\sqrt{2}} \int_{t_0}^{t_0+L} dt \sqrt{\frac{\hat{q}_{\text{eff}}}{2\omega}} \\
&= \sqrt{\frac{\hat{q}_{\text{eff}}}{4\omega}} [t_0 + L_{\text{eff}} - t_0] \\
&= \sqrt{\frac{\hat{q}_{\text{eff}} L_{\text{eff}}^2}{4\omega}}.
\end{aligned} \tag{4.37}$$

The small ω expansion for the power-law is:

$$\ln|c(t_0)| = \frac{1}{\sqrt{2}} \int_{t_0}^{t_0+L} dt \sqrt{\frac{\hat{q}(t)}{2\omega}} = \sqrt{\frac{\hat{q}_0}{4\omega}} \int_{t_0}^{t_0+L} dt \sqrt{\left(\frac{t_0}{t}\right)^a}. \quad (4.38)$$

Equate the two asymptotic solutions and take the square to find an expression for \hat{q}_{eff} in terms of \hat{q}_0 and a . Thus, the new scaling law is:

$$\begin{aligned} \frac{\hat{q}_{\text{eff}} L_{\text{eff}}^2}{4\omega} &= \left[\sqrt{\frac{\hat{q}_0}{4\omega}} \int_{t_0}^{t_0+L} dt \sqrt{\left(\frac{t_0}{t}\right)^a} \right]^2, \\ \hat{q}_{\text{eff}} L_{\text{eff}}^2 &= \hat{q}_0 \left[\int_{t_0}^{t_0+L} dt \sqrt{\left(\frac{t_0}{t}\right)^a} \right]^2. \end{aligned} \quad (4.39)$$

The accuracy of this scaling law is shown in Figure 4.10. In the same fashion as for the previous scaling law, I have chosen a value of $\hat{q}_{\text{eff}} = 3.2$ in arbitrary units, and found the corresponding \hat{q}_0 and a using Eq.(4.39). In the very low ω -regime, this scaling law works to a good accuracy. However, this approximation gets very bad in the large ω -regime. This can also be understood by observing the bigger difference of ω_{cr} , compared to the ones found by the previous scaling (see Figure 4.9). If the critical values were 1, the spectra would have been perfectly overlapped. The bigger the difference, the worse accuracy one gets.

4.6.3 Large ω scaling

In the same fashion as the previous scaling law was derived, the same will be done using the large ω expansion, Eq.(4.27). Solving the integral for the brick, we find

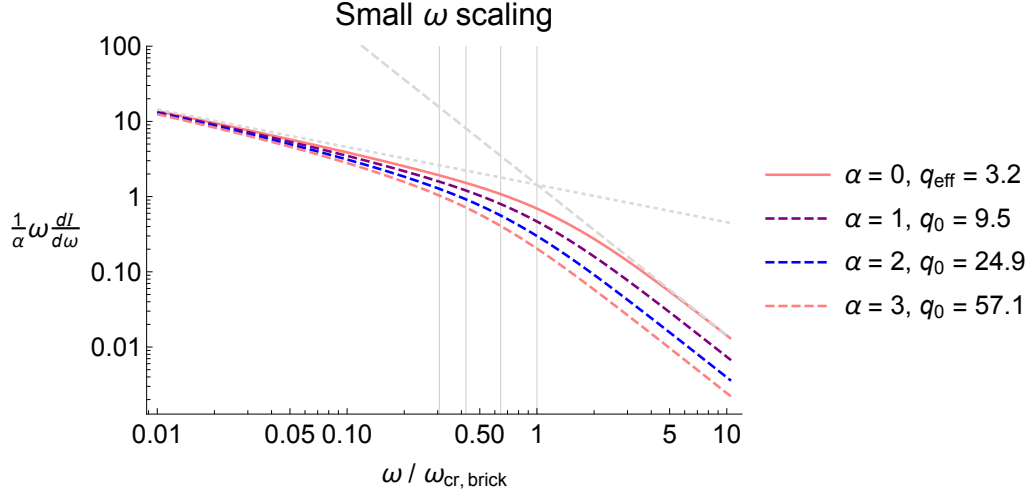


Figure 4.10: The medium-induced spectrum for three different values of a compared to the corresponding brick spectrum found using Eq.(4.39). The x -axis is given in $\omega/\omega_{cr,brick}$. The asymptotic solutions are shown for $a = 0$ (brick) and the intersection point of these, which occurs at 1, is our definition of $\omega_{critical}$. The asymptotic solutions are shown for $a = 0$ (brick) and the intersection point of these, which occurs at 1, is our definition of ω_{cr} . The dotted lines are the spectra found using the analytic solution for a power-law using the corresponding values of \hat{q}_0 and a . The solid line is the corresponding scaled spectra using \hat{q}_{eff} found by Eq.(4.39). For very small energies, this scaling shows good accuracy. The opposite end of the spectra gets very bad, which can be understood by how much the critical values differ from 1. If they were exactly 1, the spectra would overlap perfectly.

the large ω expansion to be:

$$\begin{aligned}
\ln|c(t_0)|^{(brick)} &= \frac{1}{2} \left[\int_{t_0}^{t_0+L} dt(t-t_0)|\omega_0^2(t)| \right]^2 \\
&\quad - \int_{t_0}^{t_0+L} dt(t-t_0)|\omega_0^2(t)| \int_t^{t_0+L} dt'(t'-t)|\omega_0^2(t')| \\
&= \frac{1}{2} \left[\int_{t_0}^{t_0+L} dt(t-t_0) \frac{\hat{q}_{eff}}{2\omega} \right]^2 \\
&\quad - \int_{t_0}^{t_0+L} dt(t-t_0) \frac{\hat{q}_{eff}}{2\omega} \int_t^{t_0+L} dt'(t'-t) \frac{\hat{q}_{eff}}{2\omega} \\
&= \left(\frac{\hat{q}_{eff}}{2\omega} \right)^2 \left(\frac{1}{2} \frac{L_{eff}^4}{4} - \frac{L_{eff}^4}{24} \right) = \frac{\hat{q}_{eff}^2 L_{eff}^4}{48\omega^2}. \tag{4.40}
\end{aligned}$$

The large ω expansion for the power-law gives:

$$\begin{aligned}
\ln|c(t_0)| &= \frac{1}{2} \left[\frac{1}{2\omega} \int_{t_0}^{t_0+L} dt(t-t_0)\hat{q}(t) \right]^2 \\
&\quad - \frac{1}{4\omega^2} \int_{t_0}^{t_0+L} dt(t-t_0)\hat{q}(t) \int_t^{t_0+L} dt'(t'-t)\hat{q}(t') \\
&= \frac{1}{4\omega^2} \left[\frac{1}{2} \left[\int_{t_0}^{t_0+L} dt(t-t_0)\hat{q}(t) \right]^2 \right. \\
&\quad \left. - \int_{t_0}^{t_0+L} dt(t-t_0)\hat{q}(t) \int_t^{t_0+L} dt'(t'-t)\hat{q}(t') \right]. \tag{4.41}
\end{aligned}$$

The power-law considered, for which $\hat{q}(t) = \hat{q}_0(t_0/t)^a$, can be simplified further by placing \hat{q}_0^2 in front, and keep the time-dependent term, $(t_0/t)^a$, in the integrals. To keep this as general as possible, this simplification will be done in the last step of the following equation. Equating the two expansions, one gets the following relation between \hat{q}_{eff} and \hat{q}_0 :

$$\frac{\hat{q}_{\text{eff}}^2 L_{\text{eff}}^4}{12} = \frac{1}{2} \left[\int_{t_0}^{t_0+L} dt(t-t_0)\hat{q}(t) \right]^2 - \int_{t_0}^{t_0+L} dt(t-t_0)\hat{q}(t) \int_t^{t_0+L} dt'(t'-t)\hat{q}(t'), \tag{4.42}$$

$$\begin{aligned}
\frac{\hat{q}_{\text{eff}}^2 L_{\text{eff}}^4}{6} &= \hat{q}_0^2 \left[\left(\int_{t_0}^{t_0+L} dt(t-t_0) \left(\frac{t_0}{t}\right)^a \right)^2 \right. \\
&\quad \left. - 2 \int_{t_0}^{t_0+L} dt(t-t_0) \left(\frac{t_0}{t}\right)^a \int_t^{t_0+L} dt'(t'-t) \left(\frac{t_0}{t'}\right)^a \right], \tag{4.43}
\end{aligned}$$

where Eq.(4.42) is a general expression only involving some time-dependent transverse momentum broadening coefficient, $\hat{q}(t)$, yet to be defined. The scaling law for the power-law considered in this chapter, for which $\hat{q}(t) = \hat{q}_0(t_0/t)^a$, is given by Eq.(4.43).

The results are provided in Figure 4.11. Given that this scaling law is derived using the large ω expansion, it is not surprising that its accuracy in the large ω regime is very high. If the different combinations of \hat{q}_0 and a would give the same ω_{cr} , they would have given the same spectrum. Thus, by observing of how close these values are (seen as gray, vertical lines in the figure), can be seen as a way of measuring the accuracy of the scaling law.

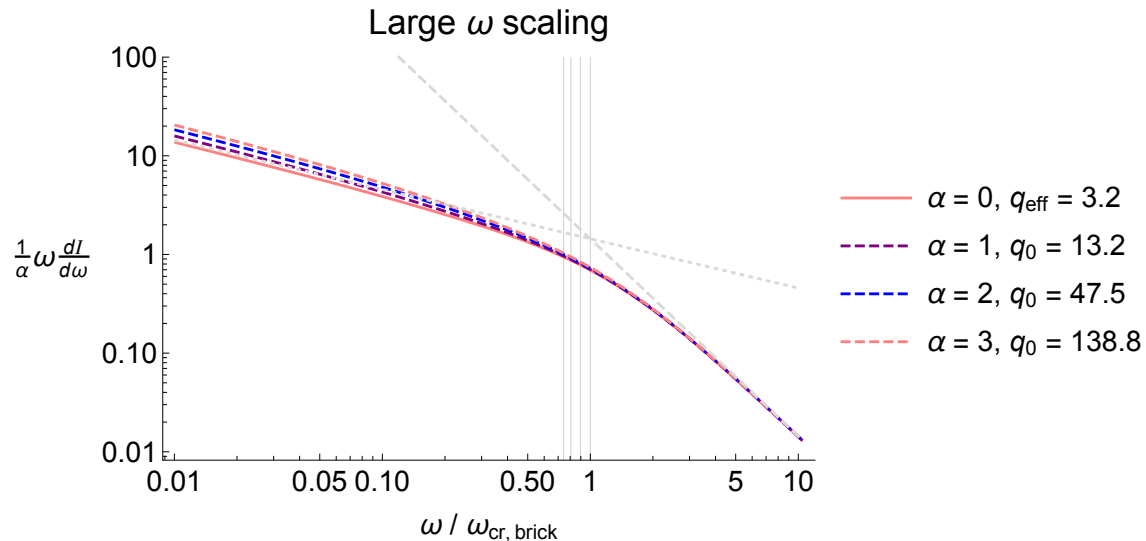


Figure 4.11: The medium-induced spectrum for three different values of a compared to the corresponding brick spectrum found using Eq.(4.43). The x -axis is given in $\omega/\omega_{cr,brick}$. The asymptotic solutions are shown for $a = 0$ (brick) and the intersection point of these, which occurs at 1, is our definition of ω_{cr} . The spectra using this scaling law is a very good approximation when considering the regime around the critical value, ω_{cr} and higher energy. One can also note that the different ω_{cr} corresponding to different a are closer than those found by using Salgado and Wiedemann as well as the one found using small ω expansion.

4.6.4 Comparing different scaling laws

The accuracy of the three scaling laws mentioned in the previous section will now be discussed further and compared. Fig. 4.12 shows the deviation from the power-laws using the three different scaling laws. The deviation is found by the absolute value of the difference between the corresponding spectra. At first glance, one can divide the spectrum of Fig. 4.12 into three main regimes: ($\omega < 0.065 \omega_{cr}$), ($0.065 \omega_{cr} < 0.65 \omega_{cr}$) and ($\omega > 0.65 \omega_{cr}$). Note that these values are only approximate. These values are marked with gray, vertical lines together with a line at 1 corresponding to the critical energy. In the low ω regime, the scaling law derived using the small ω expansion gives the minimum difference. Thus, in this regime, this scaling law will provides the most accurate approximation of the spectra. In the region $0.065 \omega_{cr} < 0.65 \omega_{cr}$, the scaling law provided by Salgado and Wiedemann has the best accuracy and is shown in gray. The dip in this line is because these spectra overlap around the value $\omega = 0.4 \omega_{cr}$

(see Fig. 4.9). For higher energies than $\omega > 0.65\omega_{cr}$, the best approximation is given by the scaling law derived using the large ω expansion. The difference between the spectra drops rapidly towards zero after the critical value, which means that the approximation basically overlaps the spectrum at high energies.

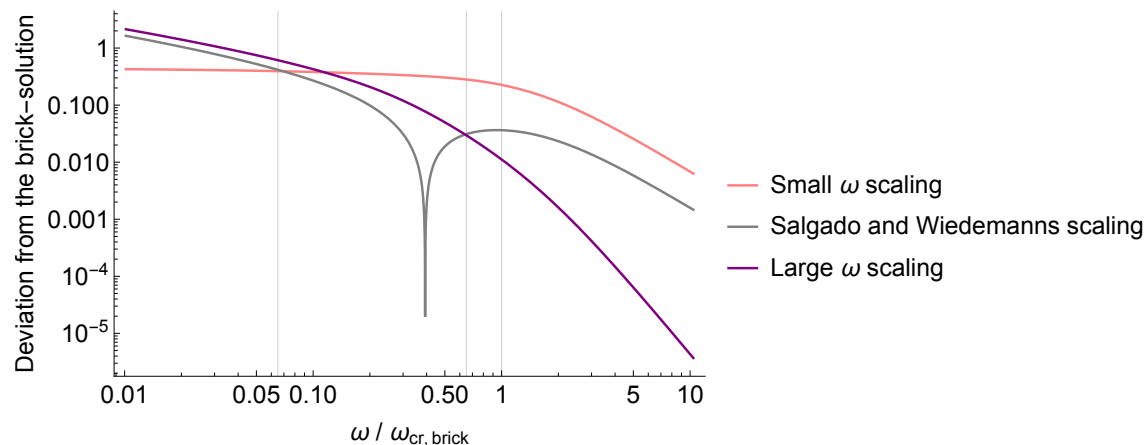


Figure 4.12: Comparison of the different scaling laws shown in a LogLogPlot. The plot shows deviation from the brick-profile using the different scaling laws from Section 4.6. The dip in the gray line is where the scaled function is overlapping/equals that of the brick (see Figure 4.9). The x -axis is given in the ratio $\omega/\omega_{critical}$. The vertical lines at 0.065 and 0.65 mark the three approximate parts of the spectrum where different scaling laws provide the highest accuracy. By our definition, the line at 1 is where $\omega = \omega_{cr,brick}$.

Another way of determining the accuracy of the different scaling laws is to look at the critical energy, ω_{cr} for the different values of a . This can be seen by comparing the separation of the vertical gray lines in Figures 4.9, 4.10 and 4.11. The scaling using the small ω expansion is clearly the worst. The critical values are very far apart, and this is also reflected by how bad the approximations gets at high energy. The two other scaling laws, on the other hand, provides much better values for ω_{cr} . In fact, the values derived from large ω expansion seems to be a little bit closer to $\omega_{cr,brick}$. Even though this approximation gets slightly worse at low energies, at higher energies this scaling law provides more accurate spectra compared to those from Salgado and Wiedemann.

Summary and Outlook

In this thesis, important features of quantum chromodynamics have been introduced and derived. The allowed self-interaction between the force carriers, due to the colour charge, led to additional Feynman diagrams. These explain the allowed interactions between gluons in the theory of strong interactions. Gluon-gluon interactions also give rise to confinement among quarks. If one tries to separate quarks by increasing the length between them, the force between them gets stronger. Thus, no isolated quarks can be found in nature. On the other hand, by pushing them closely together, quarks can act as if they are free within a certain region. This is called asymptotic freedom.

By accelerating nuclei to relativistic energies and colliding them, quarks and gluons can exist in a new state of matter called quark-gluon plasma. A motivation for studying heavy-ion collisions is to know more about the properties of this phase and to know more about the phase diagram of QCD. From heavy-ion collisions, one acquires observables suggesting the creation of QGP in heavy-ion collisions, which is not there in smaller systems such as pp-collisions. The observables are data from final states created in the collisions. By backtracking, one can learn more about the medium that is formed during these heavy-ion collisions.

In Chapter 4, a simple formula for determining the energy-loss of a particle travelling through a medium was studied for two simple medium-profiles. The simple formula by [1] was used to find the medium-induced radiation spectrum. By looking at how the hard particle radiates gluons due to interactions with the medium, one can find how much energy it loses. The total energy-loss was found by integrating over all emitted energies. The energy-loss of a particle travelling through a medium was studied for two different medium-profiles: the time-independent brick and the time-dependent medium described by a power-law. The medium-induced radiation spectrum showed that most of the radiation comes from a large number of gluons with low energy. A few hard gluons can also be emitted. The total energy-loss

of a particle travelling through some medium will depend on the critical value, ω_{cr} , defined by the transverse momentum broadening coefficient as well as the medium size. Not surprisingly, one finds that travelling through a thicker medium will give a higher energy-loss.

For values of $a < 2$ in the time-dependent medium, the spectra looks like the one obtain by the brick. The spectra also follows closely the limiting solutions provided by [1]. A dimensional analysis suggests that around $a \geq 2$, the spectrum will look more like the asymptotic solution for small L . This is because the "strength" of the medium interactions drops so fast, that after some time it will be as if there were no medium present. Thus, by increasing the value of a will be the same as if one looked at a smaller medium.

At the end of Chapter 4, different scaling laws were studied. The deviation from the power-laws using the brick-solution with a scaled, effective broadening coefficient, \hat{q}_{eff} are shown in Figure 4.12. The scaling law derived by Salgado and Wiedemann is easy to use and gives a good accuracy over almost the whole spectrum. However, we saw that the energy-loss of a particle depends on the critical value of the emitted energy, ω_{cr} . In this part of the emitted energies, the new scaling law derived in this paper, using the large ω expansion, gave the best fit. The scaling law itself might be a bit more complicated compared to Salgado and Wiedemanns. However, this resulted in even better values (closer to the desired value of 1, if it is to overlap the time-dependent spectra) for the corresponding critical values. In the end, which scaling law is better to use really depends on which part of the spectrum one is interested in, and to what degree of accuracy is needed.

The power-law used in this paper assumed uniform distribution and interaction along the medium. If we want to apply this scaling law to the study of QGP that gets created in heavy-ion collisions, it needs to work for much more complicated profiles. QCD is not a uniform medium, but $\hat{q}(t)$ can have very different values depending on both time and space. Thus, it should actually be written as $\hat{q}(x, t)$. For future work, it can be interesting to study how complicated the time-dependent medium has to be before the scaling law breaks down. Since the two new scaling laws derived in the previous chapter worked very well for small and large energies, perhaps one could combine them in one way to create an even more accurate scaling law.

Acknowledgements

I would like to thank my supervisor Aleksi Kurkela, Associate Professor in Physics at the University of Stavanger (UiS), for interesting discussions and great guidance throughout these two last semesters. I was always welcome to ask for help, and I am grateful for all the time he has spent helping me during the work that lies behind this thesis. It has been very interesting to learn so much about a new field of study from a person of his knowledge.

I would like to express my gratitude to Alexander Karl Rothkopf, Associate Professor in Physics at the University of Stavanger (UiS), for teaching me and sharing his knowledge of quantum field theory. His passion around helping and wanting his students to succeed is inspiring.

I also wish to thank Prof. Kurkela and Prof. Rothkopf together with PhD students Daniel Alvestad, Gaurang Parkar and Gerhard Ungersbäck for a useful and educational discussion group about quantum field theory.

Last, but not least, I thank Stian Penev Ramsnes for taken the time to help me with technical issues.

Bibliography

- [1] P. B. Arnold, “Simple Formula for High-Energy Gluon Bremsstrahlung in a Finite, Expanding Medium,” *Phys. Rev. D*, vol. 79, p. 065 025, 2009. DOI: 10.1103/PhysRevD.79.065025. arXiv: 0808.2767 [hep-ph].
- [2] C. A. Salgado and U. A. Wiedemann, “A Dynamical scaling law for jet tomography,” *Phys. Rev. Lett.*, vol. 89, p. 092 303, 2002. DOI: 10.1103/PhysRevLett.89.092303. arXiv: hep-ph/0204221.
- [3] M. D. Schwartz, *Quantum Field Theory and the Standard Model*. Cambridge University Press, Mar. 2014, ch. 25+26, ISBN: 978-1-107-03473-0.
- [4] Wikimedia Common, [Online]. Available: https://commons.wikimedia.org/wiki/File:Standard_Model_of_Elementary_Particles.svg.
- [5] H. J. Rothe, *Lattice gauge theories: An Introduction*. 1992, vol. 43.
- [6] R. Aaij *et al.*, “Observation of $J/\psi p$ Resonances Consistent with Pentaquark States in $\Lambda_b^0 \rightarrow J/\psi K^- p$ Decays,” *Phys. Rev. Lett.*, vol. 115, p. 072 001, 2015. DOI: 10.1103/PhysRevLett.115.072001. arXiv: 1507.03414 [hep-ex].
- [7] —, “Observation of structure in the J/ψ -pair mass spectrum,” *Sci. Bull.*, vol. 65, no. 23, pp. 1983–1993, 2020. DOI: 10.1016/j.scib.2020.08.032. arXiv: 2006.16957 [hep-ex].
- [8] W. Busza, K. Rajagopal, and W. van der Schee, “Heavy Ion Collisions: The Big Picture, and the Big Questions,” *Ann. Rev. Nucl. Part. Sci.*, vol. 68, pp. 339–376, 2018. DOI: 10.1146/annurev-nucl-101917-020852. arXiv: 1802.04801 [hep-ph].
- [9] D. H. Rischke, “The Quark gluon plasma in equilibrium,” *Prog. Part. Nucl. Phys.*, vol. 52, pp. 197–296, 2004. DOI: 10.1016/j.ppnp.2003.09.002. arXiv: nucl-th/0305030.
- [10] C. Schmidt and S. Sharma, “The phase structure of QCD,” *J. Phys. G*, vol. 44, no. 10, p. 104 002, 2017. DOI: 10.1088/1361-6471/aa824a. arXiv: 1701.04707 [hep-lat].

- [11] Y. Kim and D. Yi, “Holography at work for nuclear and hadron physics,” *Adv. High Energy Phys.*, vol. 2011, p. 259 025, 2011. DOI: 10.1155/2011/259025. arXiv: 1107.0155 [hep-ph].
- [12] G. Policastro, D. T. Son, and A. O. Starinets, “The Shear viscosity of strongly coupled N=4 supersymmetric Yang-Mills plasma,” *Phys. Rev. Lett.*, vol. 87, p. 081 601, 2001. DOI: 10.1103/PhysRevLett.87.081601. arXiv: hep-th/0104066.
- [13] R. S. Bhalerao, “Relativistic heavy-ion collisions,” in *1st Asia-Europe-Pacific School of High-Energy Physics*, Mar. 2014. DOI: 10.5170/CERN-2014-001.219. arXiv: 1404.3294 [nucl-th].
- [14] M. Brigante, H. Liu, R. C. Myers, S. Shenker, and S. Yaida, “The Viscosity Bound and Causality Violation,” *Phys. Rev. Lett.*, vol. 100, p. 191 601, 2008. DOI: 10.1103/PhysRevLett.100.191601. arXiv: 0802.3318 [hep-th].
- [15] T. D. Cohen, “Is there a ‘most perfect fluid’ consistent with quantum field theory?” *Phys. Rev. Lett.*, vol. 99, p. 021 602, 2007. DOI: 10.1103/PhysRevLett.99.021602. arXiv: hep-th/0702136.
- [16] G. Nijs, W. van der Schee, U. Gürsoy, and R. Snellings, “Bayesian analysis of heavy ion collisions with the heavy ion computational framework Trajectum,” *Phys. Rev. C*, vol. 103, no. 5, p. 054 909, 2021. DOI: 10.1103/PhysRevC.103.054909. arXiv: 2010.15134 [nucl-th].
- [17] M. E. Peskin and D. V. Schroeder, *An Introduction to quantum field theory*. Reading, USA: Addison-Wesley, 1995, ch. 15+16, ISBN: 978-0-201-50397-5.
- [18] J. N. Guenther, “Overview of the QCD phase diagram: Recent progress from the lattice,” *Eur. Phys. J. A*, vol. 57, no. 4, p. 136, 2021. DOI: 10.1140/epja/s10050-021-00354-6. arXiv: 2010.15503 [hep-lat].
- [19] B. B. Back, “Studies of multiplicity in relativistic heavy-ion collisions,” *J. Phys. Conf. Ser.*, vol. 5, R. A. Fini, B. Ghidini, V. Lenti, and T. Virgili, Eds., pp. 1–16, 2005. DOI: 10.1088/1742-6596/5/1/001. arXiv: nucl-ex/0411012.
- [20] S. Floerchinger. (). “Heavy ion physics 1 and 2,” [Online]. Available: https://indico.cern.ch/event/381289/contributions/1807997/attachments/1150639/1657352/Floerchinger_HeavyIons_L1L2v2.pdf. (Lecture notes, 08.09.2015).
- [21] S. Masciocchi, “Electromagnetic and hadronic calorimeters,” 2017. [Online]. Available: https://www.physi.uni-heidelberg.de/~sma/teaching/GraduateDays2017/sma_Detectors_4_Calorimeters.pdf.
- [22] V. Khachatryan *et al.*, “Charged-particle nuclear modification factors in PbPb and pPb collisions at $\sqrt{s_{NN}} = 5.02$ TeV,” *JHEP*, vol. 04, p. 039, 2017. DOI: 10.1007/JHEP04(2017)039. arXiv: 1611.01664 [nucl-ex].

- [23] S. Chatrchyan *et al.*, “Observation and studies of jet quenching in PbPb collisions at nucleon-nucleon center-of-mass energy = 2.76 TeV,” *Phys. Rev. C*, vol. 84, p. 024906, 2011. DOI: 10.1103/PhysRevC.84.024906. arXiv: 1102.1957 [nucl-ex].
- [24] J. Adam *et al.*, “Enhanced production of multi-strange hadrons in high-multiplicity proton-proton collisions,” *Nature Phys.*, vol. 13, pp. 535–539, 2017. DOI: 10.1038/nphys4111. arXiv: 1606.07424 [nucl-ex].
- [25] J. Cleymans, I. Kraus, H. Oeschler, K. Redlich, and S. Wheaton, “Statistical model predictions for particle ratios at $s(\text{NN})^{1/2} = 5.5\text{-TeV}$,” *Phys. Rev. C*, vol. 74, p. 034903, 2006. DOI: 10.1103/PhysRevC.74.034903. arXiv: hep-ph/0604237.
- [26] P. J. Mohr, B. N. Taylor, and D. B. Newell, “CODATA Recommended Values of the Fundamental Physical Constants: 2006,” *Rev. Mod. Phys.*, vol. 80, pp. 633–730, 2008. DOI: 10.1103/RevModPhys.80.633. arXiv: 0801.0028 [physics.atom-ph].